The Astrophysical Journal, 671:781–801, 2007 December 10

A MASSIVE CLUSTER OF RED SUPERGIANTS AT THE BASE OF THE SCUTUM-CRUX ARM

Ben Davies,[1] Don F. Figer,[1] Rolf-Peter Kudritzki,[2] John MacKenty,[3] Francisco Najarro,[4] and Artemio Herrero[5]

Received 2007 April 25; accepted 2007 August 3

ABSTRACT

We report on the unprecedented red supergiant (RSG) population of a massive young cluster, located at the base of the Scutum-Crux Galactic arm. We identify candidate cluster RSGs based on 2MASS photometry and medium-resolution spectroscopy. With follow-up high-resolution spectroscopy, we use CO band-head equivalent width and high-precision radial velocity measurements to identify a core grouping of 26 physically associated RSGs—the largest such cluster known to date. Using the stars' velocity dispersion and their inferred luminosities in conjunction with evolutionary models, we argue that the cluster has an initial mass of $\sim$40,000 $M_{\odot}$ and is therefore among the most massive in the galaxy. Further, the cluster is only a few hundred parsecs away from the cluster of 14 RSGs recently reported by Figer at al.. These two RSG clusters represent 20% of all known RSGs in the Galaxy, and now offer the unique opportunity to study the presupernova evolution of massive stars, and the blue- to red-supergiant ratio at uniform metallicity. We use GLIMPSE, MIPSGAL, and MAGPIS survey data to identify several objects in the field of the larger cluster which seem to be indicative of recent regionwide starburst activity at the point where the Scutum-Crux arm intercepts the Galactic bulge. Future abundance studies of these clusters will therefore permit the study of the chemical evolution and metallicity gradient of the Galaxy in the region where the disk meets the bulge.

Subject headings: open clusters and associations: general — stars: evolution — stars: late-type — supergiants

Online material: color figures

1. INTRODUCTION

Massive stars play a pivotal role in the evolution of their host galaxies. As main-sequence (MS) O stars, they emit copious amounts of ionizing UV radiation. Their post-MS evolution is characterized by brief but extreme mass-losing episodes, such as the red supergiant (RSG), luminous blue variable (LBV), and Wolf-Rayet (W-R) phases, during which they inject the interstellar medium (ISM) with mechanical energy and chemically processed material. When they end their lives as core-collapse supernovae (SNe), they inject the ISM with heavy elements and drive shocks into their surroundings, strongly influencing subsequent local star formation.

The stellar end state, i.e., neutron star, black hole, or complete disruption, depends on the terminal mass of the star (Heger et al. 2003). In addition, the appearance of the SN explosion is thought to be linked to the progenitor. The hydrogen-poor Type Ib+c SNe are thought to have W-R progenitors, while the progenitors of many of the H-rich Type II-P have been identified as RSGs from archival *Hubble Space Telescope* (*HST*) images (Van Dyk et al. 2003; Smartt et al. 2004; Maund et al. 2004). However, the most clear-cut case of a Type II-P progenitor remains SN 1987A, which was a blue supergiant (BSG; Sonneborn et al. 1987).

Predicting the evolution of massive stars from post–main sequence to the end of their lives is notoriously problematic. It is driven by the star's mass-loss behavior, which in turn is strongly dependent on factors such as metallicity and rotation, which are poorly constrained (see review by Kudritzki & Puls 2000). Meanwhile, empirical studies of massive stellar evolution are hampered by low-number statistics, due to the steepness of the initial mass function (IMF), the short lifetimes of the stars, and the obscuring effect of the gas and dust in the Galactic plane.

Galactic young massive clusters provide us with the ideal natural laboratories in which to study massive stellar evolution. Such objects provide a coeval sample of massive stars under the constraint of uniform metallicity, while being close enough to resolve the individual stars. Unfortunately, such objects are rare. Until recently, only Westerlund 1 [Wd 1; Clark et al. 2005), the Arches Cluster (Figer et al. 2002), the Quintuplet Cluster (Figer et al. 1999), and the Galactic center (GC) cluster (Figer et al. 2004) were known to be massive enough and young enough to harbor statistically significant numbers of massive stars. Ages of these clusters range from $\sim$3 (Arches) to $\sim$5 Myr (Wd 1). Hence, while they are both young and massive enough to contain large numbers of O stars and W-Rs, they are *too* young to have similar numbers of RSGs, which are expected after $\sim$6 Myr.

Using catalogs of Galactic plane cluster candidates (Bica et al. 2003a, 2003b; Dutra et al. 2003), Figer et al. (2006, hereafter FMR06) made the discovery of an unprecedented cluster of 14 RSGs at a Galactic longitude of $l = 25^{\circ}$, hereafter known as RSGC1. At the time of discovery this object contained by far the greatest number of RSGs of all known Galactic clusters, a record previously held by NGC 7419 with five (Caron et al. 2003).

RSGC1 is located at the base of the Scutum-Crux arm, close to where it meets the Galactic bulge. It is separated by $\sim 1^{\circ}$ from another reddened cluster, Stephenson 2. In the discovery paper, Stephenson (1990) speculated that the cluster may harbor several RSGs, possibly up to 10, based on the brightness of the stars in the *I* band. The cluster was also studied by Nakaya et al. (2001) and Ortolani et al. (2002), who estimated distances of 1.5/5.9 kpc, and ages of 50/20 Myr, respectively, from optical and infrared photometry.

Here we present low- and high-resolution spectroscopy of over 40 red stars in this cluster, and combine this with 2MASS, the *Midcourse Space Experiment* (*MSX*), and GLIMPSE photometry.

[1] Chester F. Carlson Center for Imaging Science, Rochester Institute of Technology, 54 Lomb Memorial Drive, Rochester NY 14623.

[2] Institute for Astronomy, University of Hawaii, 2680 Woodlawn Drive, Honolulu, HI 96822.

[3] Space Telescope Science Institute, 3700 San Martin Drive, Baltimore, MD 21218.

[4] Instituto de Estructura de la Materia, Consejo Superior de Investigaciones Cientificas, Calle Serrano 121, 28006 Madrid, Spain.

[5] Instituto de Astrofísica de Canarias, Via Làctea S/N, E-38200 La Laguna, Tenerife, Spain.

TABLE 1

OBSERVATIONAL DATA FOR THE BRIGHTEST STARS IN THE 2MASS POINT-SOURCE CATALOG WITHIN 7′ OF THE CLUSTER CENTER

ID	S90	N01	R.A. (J2000.0)	DECL. (J2000.0)	J	H	K_s	OBSERVATION DATE	
								NIRSPEC	IRMOS
(1)	(2)	(3)	(4)	(5)	(6)	(7)	(8)	(9)	(10)
1			18 39 02.4	−06 05 10.6	7.15	4.698	2.900	2006 Aug 12	2006 Apr 17
2	2		18 39 19.6	−06 00 40.8	6.899	5.045	4.117	2006 May 5	
3	10		18 39 24.6	−06 02 13.8	7.273	5.458	4.499	2006 May 5	
4			18 39 29.5	−05 57 16.6	7.906	5.705	4.647	2006 Aug 12	2006 Apr 18
5			18 39 08.1	−06 05 24.4	8.532	6.054	4.822	08/12	2006 Apr 17
6	1		18 39 18.4	−06 00 38.4	7.717	5.919	5.062	2006 May 5	
7			18 39 38.9	−06 02 14.5	7.585	5.867	5.090	2006 Aug 12	2006 Apr 20
8	4		18 39 19.9	−06 01 48.1	7.817	6.015	5.106	2006 May 5	
9			18 39 06.8	−06 03 20.3	8.569	6.308	5.233	08/12	2006 Apr 17
10		1102	18 39 14.7	−06 01 36.6	8.218	6.214	5.244	2006 May 5	
11		1180	18 39 18.3	−06 02 14.3	8.354	6.207	5.256	2006 May 5	
12			18 38 51.4	−06 00 22.8	7.221	5.943	5.354	...	
13		1230	18 39 17.7	−06 04 02.5	8.421	6.387	5.439	2006 Aug 12	2006 Apr 17
14	5		18 39 20.4	−06 01 42.6	8.222	6.355	5.443	2006 May 5	
15	6		18 39 22.4	−06 01 50.1	8.129	6.346	5.513	2006 May 5	
16	8		18 39 24.0	−06 03 07.3	8.235	6.444	5.597	2006 May 5	
17			18 39 15.1	−06 05 19.1	8.709	6.613	5.619	2006 Aug 12	2006 Apr 17
18	7		18 39 22.5	−06 00 08.4	8.179	6.451	5.632	2006 Aug 12	
19	3		18 39 19.5	−05 59 19.4	8.282	6.584	5.801	2006 Aug 12	
20	9		18 39 24.1	−06 00 22.8	8.426	6.656	5.805	2006 Aug 12	
21		598	18 39 15.8	−06 02 05.5	9.115	6.925	5.824	2006 May 5	
22			18 39 28.9	−05 56 43.6	9.142	7.071	5.825	2006 Aug 12	2006 Apr 18
23			18 39 01.5	−06 00 59.9	10.088	7.219	5.840	2006 Aug 13	2006 Apr 20
24			18 39 30.8	−05 58 23.3	7.356	6.368	5.960	2006 Aug 12	2006 Apr 17
25			18 39 25.7	−05 58 01.1	8.911	6.965	5.975	2006 Aug 12	2006 Apr 17
26			18 39 35.1	−05 59 15.8	8.676	6.902	6.003	2006 Aug 12	2006 Apr 17
27			18 39 16.0	−06 05 03.2	9.058	7.055	6.129	2006 Aug 12	2006 Apr 17
28			18 39 16.4	−06 03 15.0	7.626	6.589	6.132	2006 Aug 12	2006 Apr 17
29			18 39 22.2	−06 02 14.7	8.608	6.877	6.146	2006 May 5	
30			18 39 23.4	−05 59 01.3	8.711	6.956	6.200	2006 Aug 12	
31		978	18 39 09.3	−06 01 06.9	9.373	7.232	6.244	2006 Aug 13	2006 Apr 20
32			18 38 53.5	−05 57 51.2	9.676	7.571	6.490	2006 Aug 13	
32b			18 38 52.8	−05 57 40.0	...	...	...	2006 Aug 13	
33			18 39 01.6	−06 04 20.4	10.359	7.861	6.581	2006 Aug 12	2006 Apr 17
34			18 39 10.0	−05 56 22.4	9.691	7.579	6.585	...	
35			18 39 17.2	−06 03 17.9	8.878	7.291	6.651	2006 Aug 12	2006 Apr 17
36			18 38 59.2	−05 59 26.0	11.133	8.142	6.655	2006 Aug 13	
37			18 39 18.3	−06 05 42.4	10.177	7.843	6.693	...	
38			18 38 53.4	−05 57 44.4	8.572	7.324	6.794	2006 Aug 13	
39			18 39 07.0	−06 05 04.4	9.695	7.764	6.846	...	2006 Apr 17
40			18 38 54.7	−06 04 08.4	10.240	7.929	6.862	...	
41			18 39 21.9	−06 02 16.5	9.452	7.781	6.904	...	
42			18 39 16.1	−06 04 58.7	12.443	8.872	6.936	...	
43			18 38 56.4	−05 57 52.2	10.621	8.118	6.947	2006 Aug 13	
44			18 38 54.4	−05 59 53.1	8.325	7.359	7.077	...	
45			18 39 40.1	−06 01 51.6	9.749	7.981	7.085	...	2006 Apr 20
46			18 39 26.8	−05 56 15.8	9.994	8.203	7.086	2006 Aug 12	2006 Apr 18
47			18 39 32.5	−06 02 21.2	9.102	7.741	7.144	...	2006 Apr 20
48			18 39 18.6	−06 07 13.7	11.873	8.841	7.242	...	
49			18 39 05.6	−06 04 26.6	14.228	9.919	7.324	2006 Aug 12	2006 Apr 17
50			18 39 02.1	−06 02 34.1	9.676	8.204	7.394	...	
51			18 39 20.4	−05 56 07.1	12.978	9.400	7.406	...	
52			18 39 23.4	−06 02 15.9	11.274	8.763	7.419	2006 May 5	
53			18 39 14.5	−05 56 15.9	9.463	8.011	7.420	...	
54			18 39 11.8	−05 58 33.7	9.746	8.169	7.462	...	
55			18 39 12.1	−05 59 01.8	10.419	8.396	7.471	...	
56			18 39 41.0	−05 59 10.8	10.521	8.399	7.479	...	
57			18 39 03.9	−05 54 32.5	12.332	9.240	7.518	...	
58			18 39 00.8	−05 59 08.2	12.261	9.086	7.522	2006 Aug 13	
59			18 38 50.1	−05 59 25.6	9.285	8.109	7.635	...	
60			18 39 18.1	−06 03 08.3	10.756	8.721	7.679	2006 Aug 12	
61			18 39 11.8	−06 03 15.3	10.972	8.721	7.685	2006 Aug 12	2006 Apr 17

TABLE 1—*Continued*

ID (1)	S90 (2)	N01 (3)	R.A. (J2000.0) (4)	Decl. (J2000.0) (5)	J (6)	H (7)	K_s (8)	Observation Date NIRSPEC (9)	Observation Date IRMOS (10)
62.....			18 39 28.6	−05 59 50.2	11.147	8.934	7.692	...	
63.....			18 39 30.1	−05 57 26.9	10.799	8.732	7.717	...	2006 Apr 18
64.....			18 39 28.5	−06 06 43.6	9.246	8.148	7.749	...	
65.....			18 39 06.3	−06 05 22.2	12.850	9.520	7.767	...	2006 Apr 17
66.....			18 39 13.4	−05 55 18.0	10.927	8.787	7.768	...	
67.....			18 38 54.7	−05 56 55.2	13.924	9.788	7.791	...	
68.....			18 39 04.5	−06 06 13.4	11.298	8.904	7.806	...	
69.....			18 38 54.8	−06 04 45.3	13.447	9.676	7.886	...	
70.....			18 39 25.4	−06 07 17.6	9.542	8.370	7.896	...	
71.....			18 38 46.8	−06 01 23.8	12.651	9.446	7.903	...	
72.....			18 39 16.2	−06 03 07.2	12.196	9.506	7.920	2006 Aug 12	

Notes.—Stars are indexed according to their K_s-band magnitudes (col. 1). Col. (2) and (3) denote identifications in the previous studies of Stephenson (1990) and Nakaya et al. (2001). Cols. (4) and (5) list the J2000.0 coordinates of each star; units of right ascension are hours, minutes, and seconds, and units of declination are degrees, arcminutes, and arcseconds. The 2MASS photometry is listed in cols. (6)–(8). The NIRSPEC and IRMOS observation dates are listed in cols. (9) and (10). Note that star 32b is not resolved in 2MASS due to its proximity to star 32.

We show from high-precision radial velocity measurements and IR photometry that the cluster, hereafter known as RSGC2, is host to 26 RSGs, by far the largest known population in the Galaxy. We use this velocity information, in conjunction with the stars' spectra and stellar evolution models, to better constrain the distance and age of the cluster.

Between them RSGC1 and RSGC2 are host to ∼20% of all known RSGs in the Galaxy, and now offer us the opportunity to study a coeval sample of Type II-P SN progenitors, as well as the BSG/RSG ratio important in constraining stellar evolutionary models, at uniform metallicity. Further, the location of the clusters within the Galaxy will allow future metallicity studies to probe the apparent chemical discontinuity observed to exist between the Galactic disk and bulge (see, e.g., Ramírez et al. 2000; Smartt et al. 2001; Najarro et al. 2004).

We begin in § 2 with a description of our observations, including target selection, data reduction, and analysis techniques. We present the results of the data analysis in § 3, and argue which of the stars observed are members of the cluster. In § 4 we estimate the cluster age and mass, before discussing the two remarkable Scutum-Crux RSGCs in the context of other massive Galactic clusters, and their significance in the study of various aspects of stellar/galactic evolution.

2. OBSERVATIONS AND DATA REDUCTION

2.1. *Target Selection and Strategy*

For a coeval population of stars, RSGs are typically ∼4 mag brighter in the K band than any other stars in the cluster. Therefore, in order to identify potential RSGs, we compiled a list of candidate stars within an 7′ radius of the cluster center (as defined by Stephenson 1990) based on their K_s-band magnitudes in the Two Micron All Sky Survey (2MASS) point-source catalog (Cutri et al. 2003).

A key spectral diagnostic for late-type stars is the CO bandhead feature at 2.295 μm. As shown in FMR06, the feature is evident in spectral type G and later, and is extremely prominent in M-type stars. Further, the feature is stronger in supergiants than giants and dwarfs. To identify those stars with CO absorption, we observed the brightest 50 stars in our target list, as well as others, with IRMOS (Infra-Red Multi-Object Spectrograph; MacKenty et al. 2003) at the KPNO 4 m, during 2006 April.

It is likely that this CO subsample of stars is contaminated by foreground/unrelated M dwarfs and giants. To determine which of our sample are physically related, we obtained follow-up high-resolution spectroscopic data of the CO feature to measure high-precision radial velocities of the stars. These data were taken with NIRSPEC, the cross-dispersed echelle spectrograph at the Keck II telescope (McLean et al. 1998), during two observing runs in 2006 May and August. In total we observed all but one of the brightest 33 stars, as well as 11 others. As is shown in § 3, the fainter stars of the sample are more likely to be foreground objects and not supergiants; therefore, the few stars we missed will not have a significant impact on our conclusions.

Table 1 lists the brightest 72 stars within a 7′ radius of the cluster center, together with their 2MASS photometry and the dates observed. The stars are indexed in order of their K_s-band magnitude; also listed are any identification in Stephenson (1990) and Nakaya et al. (2001). A 2MASS K_s-band image of RSGC2 is shown in the top panel of Figure 1, and the bottom panel shows a finding chart for the stars. Both the K-band image and the finding chart are centered on the approximate center of the cluster, $18^{\rm h}39^{\rm m}20.4^{\rm s}$, $-6^\circ01'41''$ (J2000.0; star 5 in S90, star 14 in this paper).

2.2. *IRMOS Observations*

The Infrared Multi-Object Spectrograph (IRMOS; MacKenty et al. 2003), uses a micromirror array of $\sim 10^6$ elements. Synthetic "slits" can be defined by switching selected mirrors of the array into the "on" position. We split the cluster up into subfields, and using preimaging data defined a series of slits at the positions of stars in the current field. We interwove science frames with "all-off" frames, to make an accurate measure of the dark current and instrumental background, and took flat-field observations for each MOS configuration with a continuum lamp. We observed the A star HD 44612 as a telluric standard.

2.2.1. *IRMOS Data Reduction*

For each science frame, we subtracted the corresponding dark frame and extracted subframes containing each of the spectra. Each subframe was divided through by its associated flat field in the continuum-lamp exposures, to correct for pixel-to-pixel variations in sensitivity. Sky subtraction was done by interpolation of the regions either side of the star, and the spectra were optimally

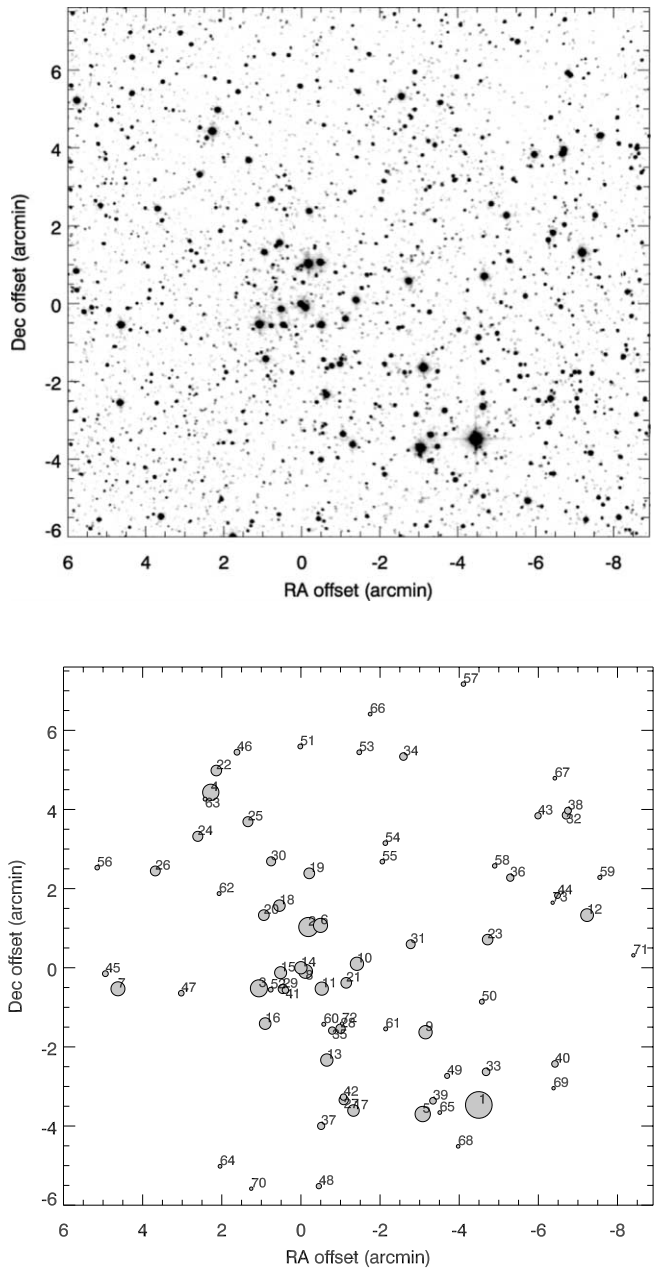

FIG. 1.—2MASS *K*-band image of RSGC2 (*top*) and finding chart (*bottom*). Coordinates are centered on $18^{h}39^{m}20.4^{s}$, $-06^{\circ}01'\ 41''$ (J2000.0), following Stephenson (1990). The sizes of the plotting symbols scale linearly with *K*-band magnitude.

extracted by weighting the pixels according to the strength of the signal above the sky background. Wavelength calibration was done using the sky emission lines and telluric absorption features. The Brγ absorption was removed from the telluric standard via linear interpolation of the continuum, and the resulting spectrum used to correct for telluric absorption.

2.3. *NIRSPEC Observations*

We used the instrument in high-resolution mode, with the NIRSPEC-7 filter, in conjunction with the $0.576'' \times 24''$ slit. The dispersion angle was set to 62.53°, with cross-dispersion angle set to 35.53°. This gave us a spectral resolution of $\sim$17,000 in the wavelength range of 1.9–2.4 μm.

We integrated on each star for 20 s in each of two nod positions along the slit. In addition to the cluster stars, we also observed HD 171305, a B0 V star, as a telluric standard on each night. Flat fields were taken with a continuum lamp. For wavelength calibration purposes, arc frames were taken with Ar, Ne, Xe, and Kr lamps to provide as many template lines as possible in the narrow wavelength range of each spectral order. To fully sample the wavelength regions between the spectral lines, we also observed the continuum lamp through an etalon filter.

2.3.1. *NIRSPEC Data Reduction*

Removal of sky emission, dark current, and bias offset was done by subtracting nod pairs, and images were flat-fielded with the continuum-lamp exposures. Correction for the warping of the order images on the detector ("rectification") was done following the method described in detail by Figer et al. (2003). An outline of the method is presented below.

The two-dimensional transformation matrix which corrects for the warping of the orders is known as the "rectification matrix," and must compensate for the warping in both the spatial and spectral directions. Correction in the spatial direction was found from polynomial fitting to the two offset star traces in a nod pair. In the spectral direction, we first found an initial wavelength solution by fitting a first-order polynomial to the arc lines in each order. This solution was then applied to the etalon frames, giving an estimate of the etalon-line wavelengths, and hence of the separation of the etalon plates. The wavelengths of the etalon lines were then recalculated, assuming that the wavelengths are determined by the equation $\lambda_n = t/2n$, where t is the plate separation and λ_n is the wavelength of the nth order. These recalculated wavelengths were fitted with a third-order polynomial to make a secondary estimate of the rectification matrix. This solution was applied to the arc frame, and the residuals between the measured and rest-frame wavelengths of the arc lines used to fine-tune the etalon-plate thickness.

After rectifying the data, spectra were extracted by summing the pixels across the star trace in each channel. Relative shifts in wavelength of $\lesssim$4 km s^{-1}, due to the star not being in the exact center of the slit, were corrected for by cross-correlating with a reference spectrum around the atmospheric CO_2 feature beginning at $\sim$1.95 μm. The mean shift was taken to be the slit center, and the spectra of all orders shifted accordingly.

The final absolute wavelength solution, applied to all NIRSPEC data, was accurate to better than $\pm$4 km s^{-1} across all orders, based on the residuals of the arc line wavelengths. The *internal* wavelength error between spectra, measured from the 1.95 μm CO_2 feature, was less than $\pm$1 km s^{-1}.

Cosmic-ray hits and bad pixels were corrected for by taking the ratio of individual exposures of the same object, and identifying pixels outside 5 σ of the residual spectrum. Cosmic hits were replaced with the median value of the three neighboring pixels either side. We removed the H and He I absorption features of the telluric standard via linear interpolation either side of the line. The atmospheric absorption features in the science frames were then removed by dividing through by the telluric standard. Finally, the spectra were normalized by dividing through by the median continuum value. From featureless continuum regions in the final spectra, we estimate the signal-to-noise ratio to be better than 100 for all spectra.

2.4. *Data Analysis*

2.4.1. *Temperature Estimation*

We estimate the temperatures and spectral types of the stars empirically from the equivalent width of the CO band-head feature, EW_{CO}. We calibrate this method with template spectra of red

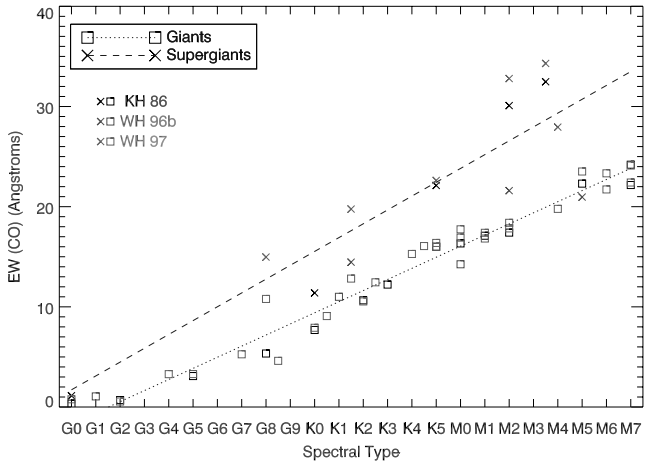

FIG. 2.—Relationship between spectral type and the equivalent width of the CO band-head feature, deduced from template spectra of Kleinmann & Hall (1986) and Wallace & Hinkle (1996b, 1997). Giants are plotted as squares, supergiants as crosses. The dotted and dashed lines show linear fits through the data. These fits were used to determine the spectral types of the target stars. [*See the electronic edition of the Journal for a color version of this figure*.]

giants and red supergiants taken from Kleinmann & Hall (1986) and Wallace & Hinkle (1996b, 1997). To do this, we define a measurement region of 2.294–2.304 μm in the rest frame. The definition of a robust local continuum region is problematic, due to the dense molecular and atomic absorption lines in this region of the spectrum. Our continuum measurements were made from the median average of the 2.288–2.293 μm region. We estimated an uncertainty on the EW_{CO} measurement by making small adjustments in the definition of the continuum region and checking the repeatability. We found that the measurements were stable to around 1 Å, or $\sim$5%.

Figure 2 shows the correlation between spectral types of the template stars and EW_{CO} as measured across the predefined wavelength range. It can be seen that the relationship between the two is approximately linear, while for a given spectral type supergiants tend to show stronger CO absorption than giants. We determined the spectral types of those stars classified as supergiants from the linear fit to the literature data shown in Figure 2. For the template giants the rms scatter on the fit is $\pm$1 subtype, while the scatter is larger for the template supergiants ($\pm$2 subtypes). This is the uncertainty we adopt throughout the rest of this paper. In converting spectral type to effective temperature, we use the temperature scale recently rederived by Levesque et al. (2005).

2.4.2. *Radial Velocity Measurements*

Following the method described in detail by Figer et al. (2003), accurate radial velocities were measured by cross-correlating the complex stellar CO band-head feature beginning at $\sim$2.293 μm with that of Arcturus, from the spectrum of Wallace & Hinkle (1996a) shifted to the zero local standard of rest velocity. We experimented with using different wavelength regions for the cross-correlation, such as including/excluding the sharp edge at the blue edge, to test the robustness of the measurement. We found that our velocity measurements are stable to within $\pm$1 km s^{-1} regardless of the wavelength range used; therefore, the absolute uncertainty of any velocity measurement is dominated by the $\pm$4 km s^{-1} error in the wavelength solution.

Figer et al. (2003) concluded that this method, when applied to red giants, introduced a systematic error in the measured radial velocity as a function of EW_{CO}, and accounted for $\pm$2 km s^{-1} across the full range of observed EW_{CO}. In order to assess any impact this may have on our data, we applied the method to the high-resolution template spectra of RSGs presented in Wallace & Hinkle (1997). As these spectra are few, it was inconclusive as to whether this systematic trend of measured v_{rad} with EW_{CO} is present in our data, but if so, it would appear to be very small ($\pm$1 km s^{-1}). It does not therefore contribute significantly to the absolute uncertainty of individual radial velocity measurements. It may, however, have an impact on the internal error between measurements and become important when determining the cluster's virial mass. We will make a more comprehensive discussion of the effect of including this uncertainty in § 4.1.1.

3. RESULTS

3.1. *Spectra*

Examples of the NIR spectra are shown in Figure 3. From the IRMOS data (Fig. 3, *left*), the CO band-head absorption can clearly be seen in the spectra, implying late spectra types for the stars. Also, no stars show the "vignetting" at the edges of the *K* band, indicative of the H_2O absorption often seen in red giants

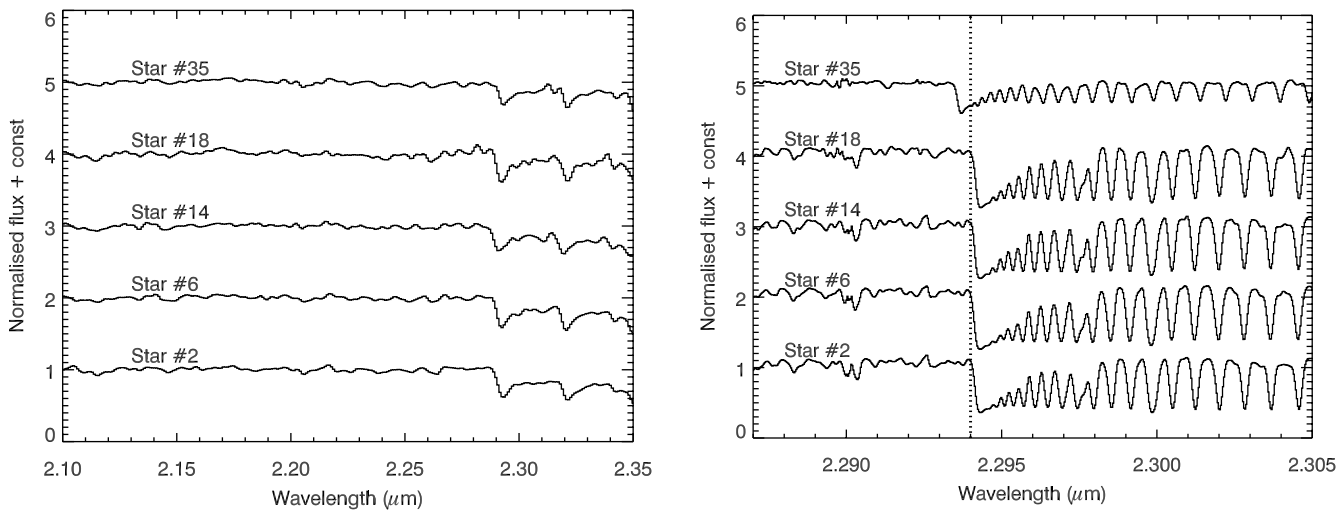

FIG. 3.—Examples of the spectra. *Left*: the IRMOS data, clearly showing the CO band-head absorption, indicative of late spectral types. *Right*: the NIRSPEC follow-up data, which highlights the radial velocity differences between star 35 and the rest.

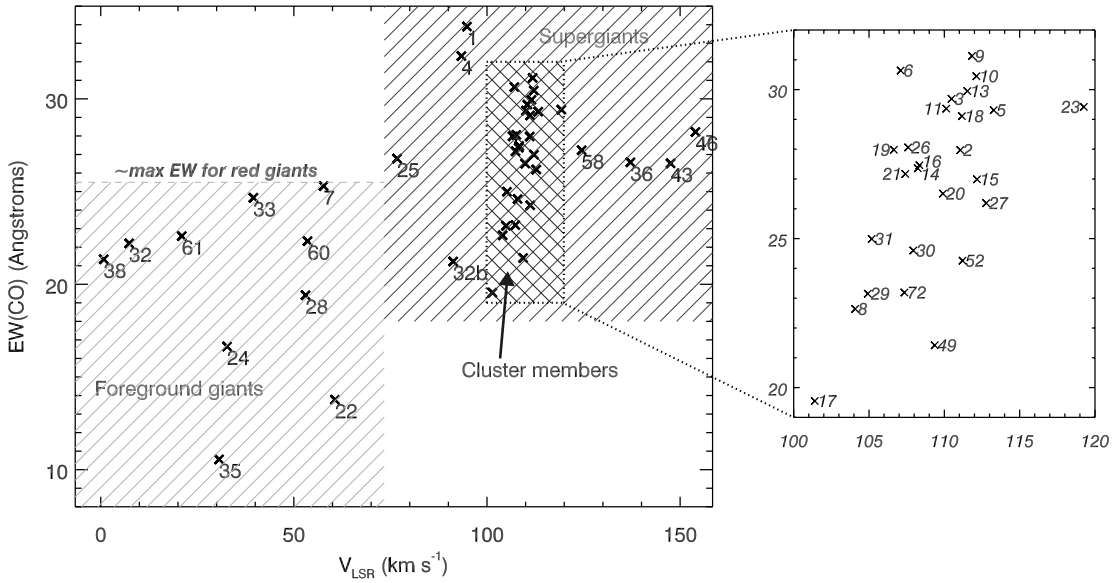

FIG. 4.—Plot of CO equivalent width vs v_{LSR} for all stars observed with NIRSPEC. Stars in the cross-hatched region have very similar velocities, and are likely to be part of the same cluster. Stars in the bottom left are probably foreground stars due to their low W_λ and much lower velocities. [*See the electronic edition of the Journal for a color version of this figure*.]

(see, e.g., atlas of Kleinmann & Hall 1986), although we note that care should be taken using this selection criterion in uncalibrated spectra. We therefore identify these stars as *candidate* RSGs. We found stars displaying these features down to $K_s \lesssim 7.5$.

The follow-up NIRSPEC data of these stars are shown in Figure 3 (*right*), and show the blue edge of the feature in greater detail. Here the difference between star 35 and the others shown in the plot is obvious—it can be seen from the blue edge of the CO band-head feature (*indicated by the dotted line*). Stars 2, 6, 14 and 18 have very similar velocities. Star 35, however, has a notable velocity shift with respect to the others. In the following section we use the radial velocity and CO equivalent width measurements to argue that, of the stars observed, a total of 26 can be readily identified as being part of a physical association of RSGs.

3.2. *Supergiants versus Foreground Stars*

The observed stars in this field separate into three categories: physically associated cluster members, unrelated foreground/background RSGs, and foreground M giants and dwarfs. Here we use the observational data from the high-resolution spectroscopy to determine which stars lie in which of these categories.

Figure 4 shows a plot of CO band-head equivalent width (W_λ) against radial velocity. Marked on the plot is the maximum EW_{CO} of the CO band-head feature observed in M giants. Any stars above this line are therefore likely to be supergiants. The plot shows that there are no stars with high EW_{CO} at low radial velocities, just as there are no stars with low EW_{CO} at high v_{rad}. We thus identify those stars in the bottom left of the plot (*red crosshatched region*) as foreground stars, while those stars in the top right, with higher v_{rad} and EW_{CO}, are identified as more distant supergiants.

Notice that within this subsample of "supergiants," there is a tight grouping of many stars with radial velocities 100–120 km s^{-1}. We identify the 26 stars within this grouping (*crosshatched region*) as being part of a physical association. A cluster member with a velocity outside this range would imply a large runaway speed, and would be unlikely to remain in the field of view for a likely cluster age of $\sim$10 Myr (see § 4.2). The supergiants outside this region are therefore probably unrelated objects in the same line of sight along the base of the Scutum-Crux arm. It will be shown later that these objects are typically more reddened, supporting this conclusion (see § 3.5). There is of course the possibility that the sample of 26 "cluster" stars is contaminated by other RSGs along the line of sight with peculiar velocities, making them appear to be part of the cluster. This number is difficult to quantify, but from the velocity spread of the "unrelated" supergiants it would seem unlikely that there more than one or two interlopers.

From these selection criteria, we determine that the cluster contains 26 RSGs—the largest associated population of RSGs discovered to date and almost twice as many as in the nearby RSGC1 described in FMR06. We also identify a further eight RSG candidates along the line of sight to RSGC2, based on the stars' high CO equivalent widths. The location of these stars within the field of the cluster is illustrated in Figure 5.

Aside from stars 12 and 34, our high-resolution observations are complete down to $K_s < 6.6$. Of the 33 stars brighter than this threshold, 23 are determined to be cluster members. Of the stars we sampled fainter than this threshold, only 3 of 11 stars were found to belong to the cluster. Hence the cluster RSGs tend to be among the brighter stars in the field, and it is unlikely that a significant number of cluster RSGs (more than one or two) were missed in our survey of the cluster.

3.3. *Spectral Types*

We take the stars classified as supergiants and determine their spectral types based on the relation to CO band-head equivalent width derived in § 2.4. The spectral types are listed in Table 2, and are plotted in a histogram in Figure 6. We plot both the entire sample of supergiants, and the subsample of cluster members (*cross-hatched*). The median spectral type for both samples is M3 I, which is in agreement with the average spectral type in the Galaxy (M2) and that of the nearby RSGC1 cluster (M3) (Elias et al. 1985; FMR06).

The median spectral type of RSGs is thought to be linked to chemical abundance. For example, RSG distribution in the low-metallicity environments of the Magellanic Clouds is significantly different to that of the Galaxy. Median spectral types of K5, M1,

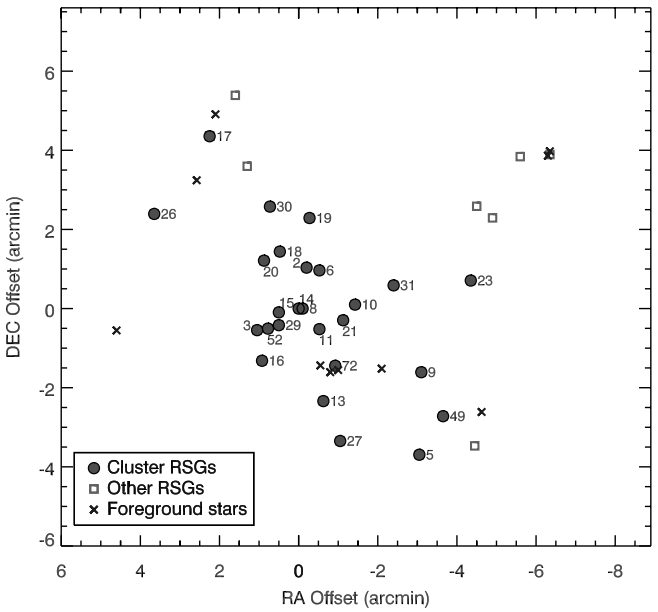

FIG. 5.—Illustration of the location of the stars belonging to the cluster and foreground/background objects. [*See the electronic edition of the Journal for a color version of this figure*.]

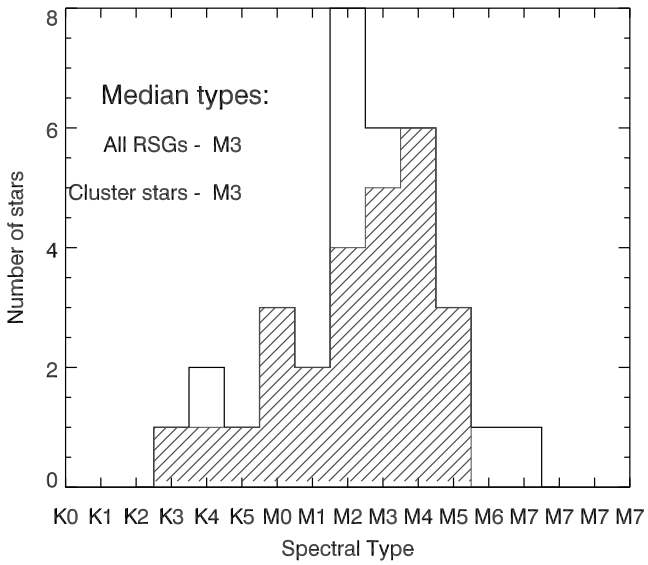

FIG. 6.—Histogram of the spectral types of the stars identified as supergiants, and the subsample determined to be "cluster members" (*cross-hatched region*). The median type of both subsamples (M3) is consistent with the nearby RSG cluster RSGC1 (M3; FMR06) and the rest of the Galaxy (M2; Elias et al. 1985). [*See the electronic edition of the Journal for a color version of this figure*.]

and M2 have been found from studies of the SMC, LMC, and the Galaxy, respectively (Humphreys 1979; Elias et al. 1985; Massey & Olsen 2003). This difference is thought to arise either from the metallicity-dependent opacity of the stellar envelope (Elias et al. 1985) or from the abundance-sensitive strengths of diagnostic molecular absorption features, e.g., TiO bands (Massey & Olsen 2003). Either way, that the median spectral types of the clusters RSGC1 and RSGC2 agree with (1) each other, and (2) those in the rest of the Galaxy, suggests that these objects have roughly similar metallicities to the Galactic average.

TABLE 2
DERIVED DATA OF THE CLUSTER STARS

ID (1)	V_{LSR} (km s^{-1}) (2)	T_{eff} (K) (3)	Spectral Type (4)	A_{K_s} (5)	M_K (6)	$\log(L_{bol}/L_\odot)$ (7)
2.....	111.1	3605 ± 147	M3	1.39 ± 0.06	$-11.12^{+0.33}_{-0.63}$	$5.22^{+0.25}_{-0.13}$
3.....	110.5	3535 ± 130	M4	1.34 ± 0.07	$-10.72^{+0.33}_{-0.63}$	$5.04^{+0.25}_{-0.13}$
5.....	113.3	3535 ± 130	M4	1.99 ± 0.07	$-11.02^{+0.33}_{-0.63}$	$5.16^{+0.25}_{-0.13}$
6.....	107.1	3450 ± 100	M5	1.17 ± 0.08	$-9.95^{+0.32}_{-0.63}$	$4.70^{+0.25}_{-0.13}$
8.....	104.1	3840 ± 135	K5	1.45 ± 0.09	$-10.23^{+0.32}_{-0.63}$	$4.94^{+0.25}_{-0.13}$
9.....	111.8	3450 ± 100	M5	1.64 ± 0.08	$-10.28^{+0.32}_{-0.63}$	$4.84^{+0.25}_{-0.13}$
10.....	112.1	3450 ± 100	M5	1.42 ± 0.08	$-10.03^{+0.32}_{-0.63}$	$4.73^{+0.25}_{-0.13}$
11.....	110.1	3535 ± 130	M4	1.42 ± 0.08	$-10.08^{+0.33}_{-0.63}$	$4.78^{+0.25}_{-0.13}$
13.....	111.5	3535 ± 130	M4	1.42 ± 0.07	$-9.85^{+0.33}_{-0.63}$	$4.69^{+0.25}_{-0.13}$
14.....	108.2	3605 ± 147	M3	1.39 ± 0.06	$-9.77^{+0.33}_{-0.63}$	$4.68^{+0.25}_{-0.13}$
15.....	112.2	3660 ± 127	M2	1.27 ± 0.06	$-9.59^{+0.32}_{-0.63}$	$4.63^{+0.25}_{-0.13}$
16.....	108.3	3605 ± 147	M3	1.25 ± 0.06	$-9.50^{+0.33}_{-0.63}$	$4.57^{+0.25}_{-0.13}$
17.....	101.4	4015 ± 130	K3	1.77 ± 0.05	$-9.99^{+0.31}_{-0.62}$	$4.90^{+0.25}_{-0.12}$
18.....	111.2	3535 ± 130	M4	1.16 ± 0.07	$-9.36^{+0.33}_{-0.63}$	$4.50^{+0.25}_{-0.13}$
19.....	106.7	3605 ± 147	M3	1.12 ± 0.06	$-9.17^{+0.33}_{-0.63}$	$4.44^{+0.25}_{-0.13}$
20.....	109.9	3660 ± 127	M2	1.30 ± 0.06	$-9.32^{+0.32}_{-0.63}$	$4.52^{+0.25}_{-0.13}$
21.....	107.4	3660 ± 127	M2	1.79 ± 0.06	$-9.81^{+0.32}_{-0.63}$	$4.71^{+0.25}_{-0.13}$
23.....	119.3	3535 ± 130	M4	2.29 ± 0.07	$-10.35^{+0.33}_{-0.63}$	$4.89^{+0.25}_{-0.13}$
26.....	107.6	3605 ± 147	M3	1.31 ± 0.06	$-9.16^{+0.33}_{-0.63}$	$4.44^{+0.25}_{-0.13}$
27.....	112.8	3660 ± 127	M2	1.45 ± 0.06	$-9.19^{+0.32}_{-0.63}$	$4.47^{+0.25}_{-0.13}$
29.....	104.9	3790 ± 130	M0	1.14 ± 0.08	$-8.86^{+0.33}_{-0.63}$	$4.38^{+0.25}_{-0.13}$
30.....	107.9	3745 ± 117	M1	1.15 ± 0.09	$-8.82^{+0.32}_{-0.63}$	$4.35^{+0.25}_{-0.13}$
31.....	105.2	3745 ± 117	M1	1.62 ± 0.09	$-9.24^{+0.32}_{-0.63}$	$4.51^{+0.25}_{-0.13}$
49.....	109.4	3920 ± 112	K4	4.58 ± 0.22	$-11.30^{+0.38}_{-0.66}$	$5.39^{+0.26}_{-0.15}$
52.....	111.2	3790 ± 130	M0	2.24 ± 0.08	$-8.72^{+0.33}_{-0.63}$	$4.32^{+0.25}_{-0.13}$
72.....	107.3	3790 ± 130	M0	2.55 ± 0.16	$-8.62^{+0.36}_{-0.64}$	$4.28^{+0.26}_{-0.14}$

NOTES.—Columns have the following meanings: (1) star ID, in order of ascending brightness in K_s; (2) radial velocity—absolute uncertainty is ±4 km s^{-1}, and internal error is ±1 km s^{-1}; (3) and (4) effective temperature and spectral type, accurate to two subtypes (temperatures taken from Levesque et al. 2005); (5) *K*-band extinction; (6) absolute magnitude; and (7) luminosity.

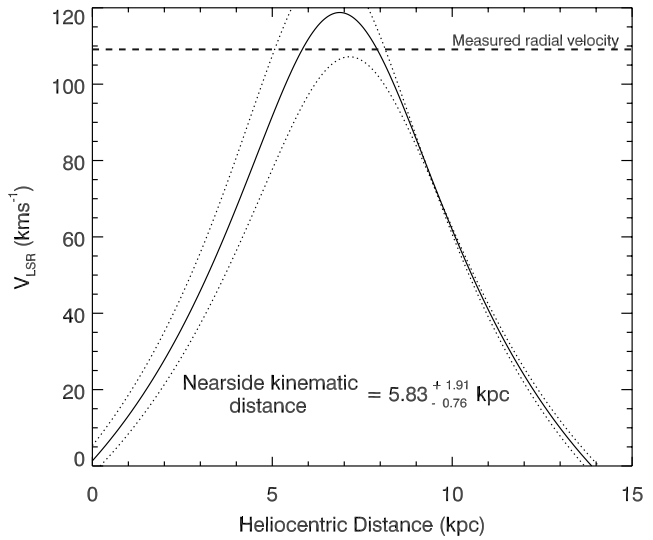

FIG. 7.—Galactic rotation curve in the direction of RSGC2, using the latest measurements collated by Kothes & Dougherty (2007; *solid line*). The dashed line represents the mean radial velocity of the cluster stars, implying the kinematic distance marked on the plot. Dotted lines illustrate the errors in this distance implied by uncertainties in the solar rotational velocity and the distance to the Galactic center. [*See the electronic edition of the Journal for a color version of this figure*.]

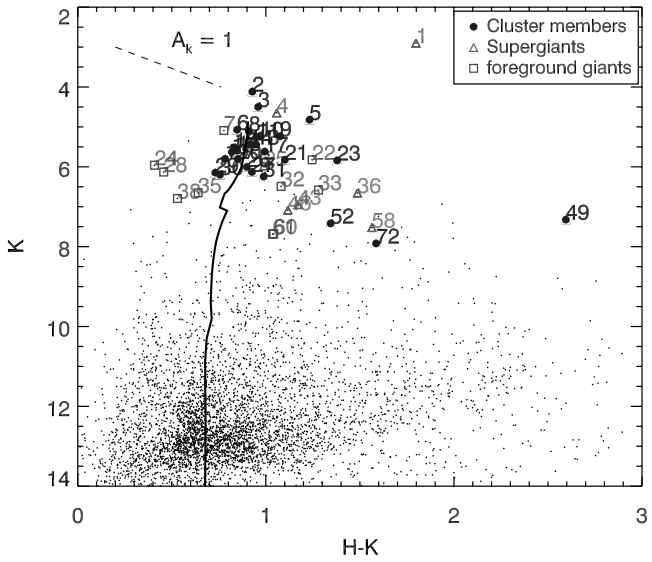

FIG. 8.—Color-magnitude diagram for all stars in the 2MASS point-source catalog within 7′ of the cluster center (*dots*). The stars observed in this paper are plotted with their ID number as indicated in the legend. The solid line represents a 12 Myr isochrone from Geneva models with solar metallicity and canonical mass-loss rates, which has been reddened according to the interstellar extinction law of Rieke & Lebofsky (1985) with $A_K = 1.47$. A reddening vector of $A_K = 1$ is also plotted. The majority of the cluster stars form a tight grouping at the top of the isochrone, the location of RSGs. [*See the electronic edition of the Journal for a color version of this figure*.]

3.4. *Cluster Distance*

The mean radial velocity of the cluster subsample is $\bar{v}_{\rm LSR} = 109.3 \pm 0.7$ km s^{-1}, with the uncertainty taken from Poisson statistics of the 26 stars. The cluster radial velocity is constrained extremely well by the large number of measurements, and the uncertainty in this value is dominated by the precision of the wavelength solution, ± 4 km s^{-1}.

In converting this radial velocity into a kinematic distance to the cluster, we are limited by the uncertainties in the Galactic rotation curve. We use the most contemporary measurements of the Galactic center distance and solar rotational velocity as compiled by Kothes & Dougherty (2007). In determining the distance to Wd 1, these authors used the Galactic center distance $D_{\rm Gal} = 7.6 \pm 0.3$ kpc, as determined by Eisenhauer et al. (2005) and the solar rotation velocity of $\Theta_\odot = 214 \pm 7$ km s^{-1}, averaged from measurements by Reid & Brunthaler (2004) and Feast & Whitelock (1997). We use these values to construct the Galactic rotation curve in the direction of RSGC2 shown in Figure 7.

From comparison with the cluster's radial velocity, we derive a kinematic distance of $5.83^{+1.91}_{-0.78}$ kpc. The uncertainties are determined from the minimal and maximal nearside distance from the errors in $D_{\rm Gal}$ and $\Theta_\odot$, and are rather large due to the location of the cluster close to the tangential point of the Galactic arm (see Fig. 7).

This distance estimate is considerably closer than the $\sim$30 kpc quoted in S90. This greater distance was determined by assuming that the cluster stars were M supergiants, then calculating the distance modulus based on their typical absolute magnitudes. However, S90 did not take into account interstellar extinction, which we determine to be $A_V = 13.1$, assuming the interstellar extinction law of Rieke & Lebofsky (1985; see § 3.5). This explains S90's large distance overestimate.

In a separate study, Nakaya et al. (2001) derived a much closer distance estimate—they isolated a sample of stars that appeared to be reddened in their I versus $R - I$ color-magnitude diagram, and assumed these were early-type stars belonging to the cluster. They then dereddened these stars to the intrinsic colors of A0 stars, deriving an extinction of $A_V = 11.4$. On fitting the "A0" stars and the S90 "red" stars with a model isochrone, they finally arrived at a distance of 1.5 kpc. In analysis of similar data, Ortolani et al. (2002) derived a distance of 6 kpc, by adding the constraint that the cluster containing so many RSGs cannot be older than $\sim$20 Myr.

While Ortolani et al.'s distance estimate is comparable to ours, these studies highlight the problematic nature of inferring cluster properties from photometry alone. Our method of determining the distance to the cluster is much more direct and relies less on assumptions of cluster membership and spectral types. From the radial velocity data, the grouping of so many stars with a velocity rms of ± 3.5 km s^{-1} is strong evidence that these stars are associated. Even allowing for a peculiar cluster velocity of ± 20 km s^{-1} from the Galactic rotation curve, due to e.g., the cluster's proximity to the Galactic bulge, this would still only imply an extra uncertainty of ± 1 kpc.

3.5. *Extinction*

Figure 8 shows a 2MASS color-magnitude diagram of all stars within 7′ of the cluster center, which is taken to be the position of star 14 (see Table 1). The stars classified as cluster members are plotted as circles, the unrelated supergiants as triangles, and the foreground stars as squares. An $A_K = 1$ reddening vector is plotted, and to guide the eye a 12 Myr solar metallicity isochrone is shown (Schaerer et al. 1993), which has been dereddened by $A_K = 1.47$ (see below).

It can be seen that the majority of the cluster stars are grouped tightly at the top of the isochrone, with no cluster stars located significantly to the left of the isochrone—consistent with the sample being uncontaminated by foreground stars. The cluster stars significantly to the right of the isochrone all lie along a reddening vector from this core grouping, suggesting that extra circumstellar reddening exists for these objects. A 2MASS color-color diagram is shown in Figure 9. Again, the majority of the

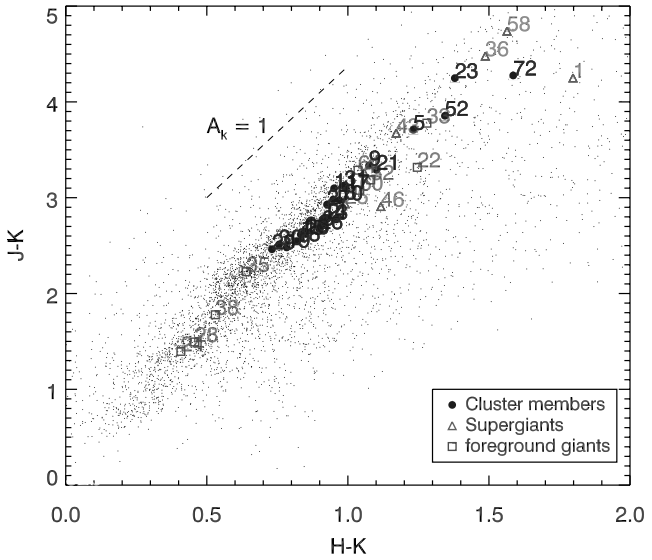

FIG. 9.—2MASS color-color diagram of the stars plotted in Fig. 8, with the same plotting symbols. A reddening vector according to $A_K = 1$ is plotted. For clarity, star 49, which lies along the reddening vector from the cluster stars with an extinction $A_K = 4.58$, is not shown. [*See the electronic edition of the Journal for a color version of this figure.*]

cluster stars form a tight grouping, and are located along the reddening vector from the origin.

To determine the extinction to the cluster, we deredden each cluster star to the intrinsic colors appropriate for their spectral type and a luminosity class of Iab, according to the survey of Galactic RSGs by Elias et al. (1985). From the $(J - K_s)$ and $(H - K_s)$ color excesses of each star, we determine the extinction A_{K_s} toward each star using the relation in Rieke & Lebofsky (1985):

$$A_{K_s} = \frac{E_{\lambda - K_s}}{(\lambda/\lambda_{K_s})^{-1.53} - 1}. \quad (1)$$

The uncertainty in each star's extinction is governed by the error in its spectral type. For ± 2 subtypes, then from the variations in RSG intrinsic colors the uncertainty in the A_K measurement of each star is about ± 0.06. This is consistent with the differences we find in the extinction measurements using the two different color-excesses (see below).

From the measurements of all the stars, we find the median extinction toward the cluster to be $A_{K_s}(J - K_s) = 1.462$, and $A_{K_s}(H - K_s) = 1.424$. These two measurements are consistent with one another, and we adopt the average of these measurements, $A_{K_s} = 1.44 \pm 0.02$, and hence $A_V = 12.9 \pm 0.2$, to be the extinction toward RSGC2. The measured extinction toward the individual stars, and the associated uncertainty determined from the error in spectral type, is listed in Table 2.

As mentioned in § 3.4, this extinction is slightly higher than that derived by Nakaya et al. (2001), who found $A_V = 11.2$. Their extinction estimate was based on the assumption that a collection of stars with particular $R - I$ colors were cluster members and had mean spectral type A0. As we know the spectral types of the stars to within a subtype, and are able to take the median of many stars which we are confident are cluster members, we consider ours to be a much more reliable estimate.

From Table 2 we see that the extinction toward the individual stars varies substantially across the field. In particular, star 49 is significantly more obscured than the rest, with $A_{K_s} = 4.6$. In the case of this star, the extra extinction can be readily associated with mid-IR excess, and is likely due to circumstellar material (see §§ 3.6 and 4.3). For the other stars with extra extinction, such as stars 5, 23, 52, and 72, an association with mid-IR excess is less obvious: stars 5 and 23 have only modest excess (see Fig. 22), while stars 52 and 72 are not detected in *MSX*. These anomalies may arise due to a combination of factors: there may be significant nonuniformity in the foreground extinction; indeed, it can be seen in Fig. 19 that there is much diffuse 8 μm emission over the field (with star 23 appearing to be spatially coincident with a dark lane); source confusion in the *MSX* images may make it impossible to detect fainter stars in crowded regions, in particular star 52, which is dwarfed by emission from the nearby star 6, may suffer from this effect; and finally we cannot entirely discount that the sample of 'cluster' stars is contaminated by one or two background stars with peculiar velocities, which are extincted by an increased column density of interstellar material (see also § 3.2).

3.6. *Luminosities and Spectral Energy Distributions*

From each stars' extinction and the kinematic distance of the cluster, we calculate absolute magnitude of each star M_{K_s}. We then interpolate the bolometric correction BC_K for each star's temperature, according to the recently rederived values of Levesque et al. (2005) to estimate their bolometric luminosities. These results are listed in Table 2.

The uncertainties in L_{bol} are derived from the quadrature sum of the errors in A_K, BC_K, and the cluster distance, D_{cl}. The errors in A_K and BC_K are governed by the precision to which we can determine the stars' spectral types, i.e., ± 2 subtypes. While these uncertainties are small compared to that in D_{cl}, we can be confident that the stars are all at the *same* distance. Hence, the propagation of the error in spectral type through to that in L_{bol} will be important when investigating the luminosity spread of the RSGs and the age of the cluster.

In addition to the 2MASS photometry, we also identify these stars in the point-source catalogs of *Spitzer* GLIMPSE (Benjamin et al. 2003) and *MSX* (Egan et al. 2001). In the GLIMPSE catalog, many of the stars are too bright to be included in the high-precision version of the catalog, and instead only appear in the less accurate, "more complete" version. In the case of the *MSX* data, despite the large beam size ($\sim 18''$), the cluster is open enough to get unambiguous photometry on several of the stars.

In Figure 22 (in the Appendix) we plot the spectral energy distributions (SEDs) of the cluster stars. We deredden the fluxes of the stars according to the extinction A_{K_s} toward each star, in combination with the interstellar extinction law for GLIMPSE and *MSX* photometry as defined in Indebetouw et al. (2005) and Messineo et al. (2005), respectively. The raw photometry is plotted as crosses, and the dereddened as filled circles.

Plotted over the photometry are blackbody curves appropriate for stars' temperatures, absolute *K*-band magnitudes and the near-side kinematic distance to the cluster. For the majority of the stars, the blackbody curves provide good fits to the dereddened photometry up to 8 μm, and validates our empirical method of determining the star's temperatures. Some objects, e.g., stars 19, 20, and 21, appear to be underluminous at 4.3 μm. This can be understood as being due to dense molecular absorption bands in this wavelength range, which can readily be seen in spectral type M model atmospheres (e.g., Fluks et al. 1994).

In the mid-IR photometry of *MSX*, many stars show evidence of significant excess emission, particularly at 12 μm. This mid-IR excess is common to RSGs, and is due to the large amounts of circumstellar oxygen-rich dust produced in this high mass-losing phase. The excess emission is illustrated in the dereddened

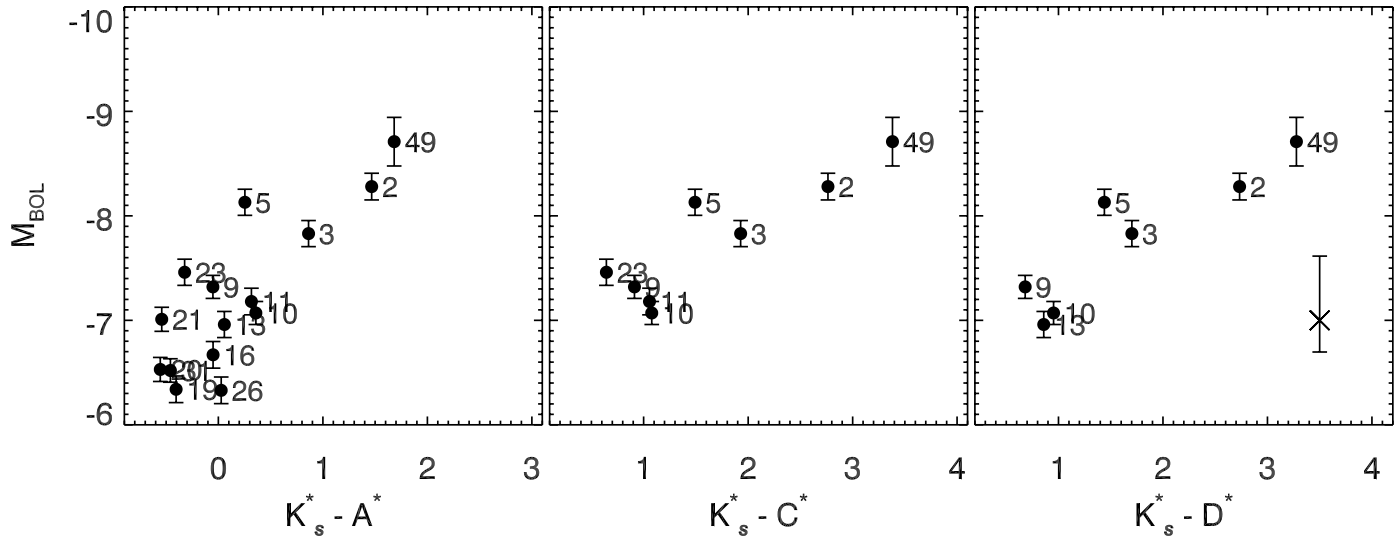

FIG. 10.—2MASS-*MSX* color-magnitude diagrams. The plots show the cluster stars' bolometric absolute magnitude against *dereddened* $K_s - (A, C, D)$ colors. Errors in $M_{\rm bol}$ are shown that discount the error in cluster distance; when included, the average error size is indicated by the error bar in the bottom right of the far-right panel. Errors in color are of order the size of the plotting symbols.

2MASS-*MSX* color-magnitude diagrams shown in Figure 10. As these unreddened photospheric colors should be approximately zero, positive 2MASS-*MSX* indices are indicative of dusty circumstellar ejecta.

Whitelock et al. (1994) showed that the $K - [12]$ color from *IRAS* photometry was directly proportional to mass-loss rate for asymptotic giant branch (AGB) stars. This color may be the most effective diagnostic for RSG mass-loss rates, as it will be influenced by the broad silicate emission feature at $\sim$9–12 μm often seen in RSG spectra (Buchanan et al. 2006). As RSGs' mass-loss rates are roughly proportional to their luminosity (van Loon et al. 2005), in Figure 10 we plot the bolometric magnitude of the stars against their $K - MSX$ colors. Each plot shows the expected $\sim$linear trend of redder colors for increasingly brighter stars, which was also seen in a sample of Galactic RSGs by Massey et al. (2005) when using the data from Josselin et al. (2000) and rederiving the stellar distances.

Another effective measure of mass-loss rate may be the $[8] - [12]$ ($MSX\ A - C$) color. This measures not just the mid-IR excess, but specifically the amount of excess caused by the broad silicate dust feature. Figure 11 plots absolute bolometric magnitude against this color, and shows a clear relation of increasing 12 μm excess with increasing luminosity. A comprehensive study of the empirically derived mass-loss rates of both the RSG clusters is beyond the scope of this work and will be the subject of a future paper.

4. DISCUSSION

4.1. *Initial Mass*

To determine the initial mass of the cluster, we use two independent methods. In § 4.1.1, we use our high-precision radial velocity measurements to infer the cluster's virial mass, under the assumption that it is in dynamical equilibrium. Second, in § 4.1.2 we compare this measurement with that determined from simulations of clusters with large numbers of RSGs, using stellar evolution models.

4.1.1. *Virial Mass*

Following the method of Mengel et al. (2002) the mass of the cluster can be measured under the assumption that it is in dynamical equilibrium. Below, we use the dispersion in radial velocity from the high-resolution spectra to estimate the dynamical mass of RSGC2. As a caveat, we note that recent work by Bastian & Goodwin (2006) suggests that young massive clusters ($\lesssim$50 Myr, $\gtrsim 10^4\,M_\odot$) can be *out* of virial equilibrium. This is caused by the violent relaxation of the cluster following the ejection of the leftover interstellar natal material by the first supernovae. As a result, the cluster mass can be overestimated by factors of up to $\sim$3 if it is incorrectly assumed to be virialized. With this in mind, we consider our derived virial mass to be an order-of-magnitude estimate.

From the radial velocity dispersion σ_v, we can estimate the dynamical cluster-mass $M_{\rm dyn}$ from the relation,

$$M_{\rm dyn} = \frac{\eta \sigma_v^2 r_{\rm hp}}{G}, \tag{2}$$

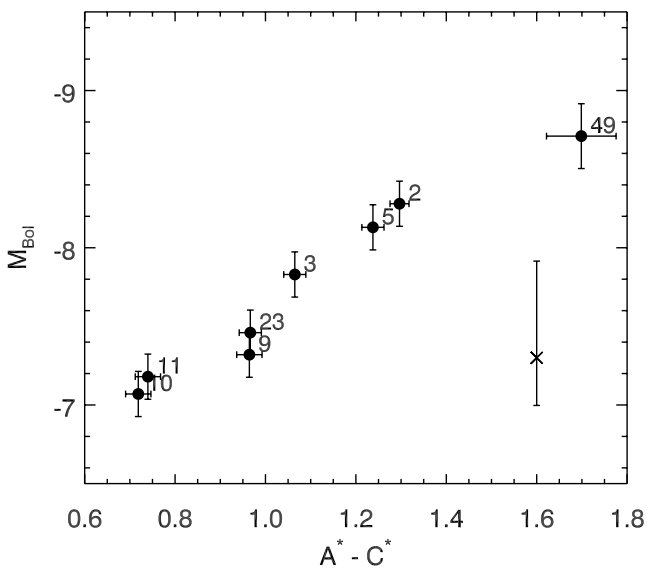

FIG. 11.—Absolute magnitude vs. unreddened $A - C$ color, illustrating the trend of increasing $[8] - [12]$ excess with luminosity for the cluster RSGs. The errors in $M_{\rm bol}$ do not include the uncertainty in the cluster distance, which is illustrated by the error bar in the lower right.

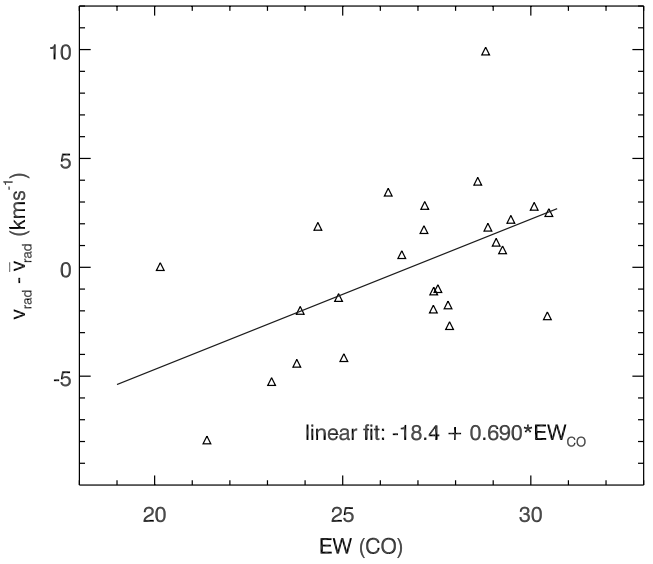

FIG. 12.—Cluster velocity dispersion as a function of equivalent width of the CO band-head feature. The slight trend may be an artifact of the method used to determine the radial velocities of the stars. [*See the electronic edition of the Journal for a color version of this figure.*]

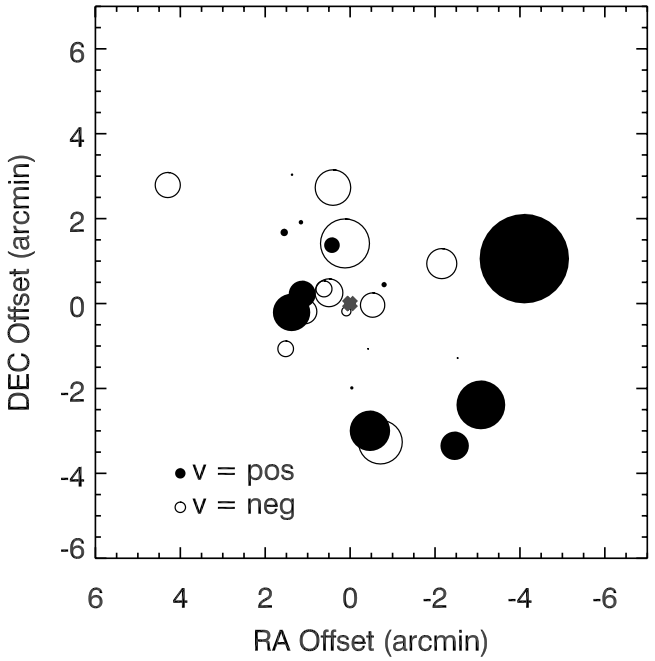

FIG. 13.—Illustration of the velocity dispersion of the stars in the cluster, when the trend with equivalent width has been corrected for and the mean cluster velocity subtracted. Symbol sizes are proportional to absolute velocity of each star, open symbols representing negative velocities and filled symbols positive velocities. The cross denotes the cluster "center," defined as the mean of the positions of the stars. [*See the electronic edition of the Journal for a color version of this figure.*]

where r_{hp} is the half-light radius of the cluster, G is the gravitational constant, and η is a constant which depends on the density and M/L as a function of radius, and is typically in the range 5–10 (for a review of the parameter η, see the introduction of Mengel et al. 2002). Below, we discuss our measurements of the parameters in this relation and estimate the dynamical mass of RSGC2.

Velocity dispersion.—As mentioned in § 2.4, the method we use to determine accurate radial velocities from the CO band-head feature was noted by Figer et al. (2003) to introduce a systematic offset as a function of W_λ when applied to red giants. This offset was determined from measurements of template red giants with well-known radial velocities. From the few template spectra of RSGs, it appears that the effect of this systematic uncertainty is less than ± 2 km s^{-1} in our data, over the full range of equivalent widths.

To investigate this further, in Figure 12, we plot the radial velocity of the "cluster-members" against their equivalent widths. The radial velocities have been shifted by the mean velocity of all the stars, to illustrate the width of the dispersion. There is an apparent trend of velocity with EW_{CO}, which has a Pearson correlation coefficient of 0.5 when a linear relationship is assumed, and is plotted over the data. There is no reason to expect a real trend to exist between velocity and equivalent width, therefore we suspect that this relation may be an artifact of our velocity-measuring method.

We investigate the effects of taking two differing estimates for the velocity dispersion: the *maximal* (observed) dispersion, and the *minimal* dispersion when the linear relation shown in Figure 12 is corrected for. In each of these estimates we have subtracted the internal uncertainty in each measurement (± 1 km s^{-1}) in quadrature. We measure the uncorrected data, i.e., that plotted in Figure 12, to have a 1 σ dispersion of 3.4 km s^{-1}, while the "corrected" velocities have 1 σ dispersion of 2.8 km s^{-1}. Therefore, we estimate that if any systematic uncertainty exists, its effect is at most $\pm 20\%$. We illustrate the "corrected" velocity dispersion of the cluster in Figure 13. The plot seems to be a trend of positive velocities in the southwest and positive in the northeast, consistent with a rotating self-gravitating cluster.

Half-light radius.—As this cluster is much more "open" than its neighbor RSGC1, the half-light radius is more difficult to define. To measure this quantity, we make the assumption that the RSGs are representative of the density profile of the cluster. Should mass segregation exist in the cluster, this will be an underestimate. Figure 14 plots the cumulative luminosity distribution of the stars in the cluster, assuming that the mean of the star positions ($18^h39^m17.^s$, $-6°2'3.3''$) is the cluster center. The plot indicates the cluster half-light radius is around $(1.9 \pm 0.3)'$. It was

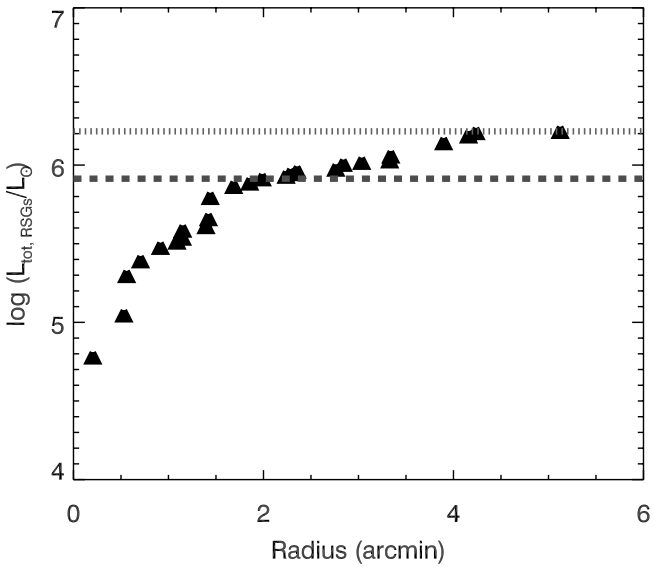

FIG. 14.—Cumulative luminosity of the cluster, assuming the mean of the star positions to be the cluster center. The maximum light and half-light are marked with dotted and dashed lines, respectively. [*See the electronic edition of the Journal for a color version of this figure.*]

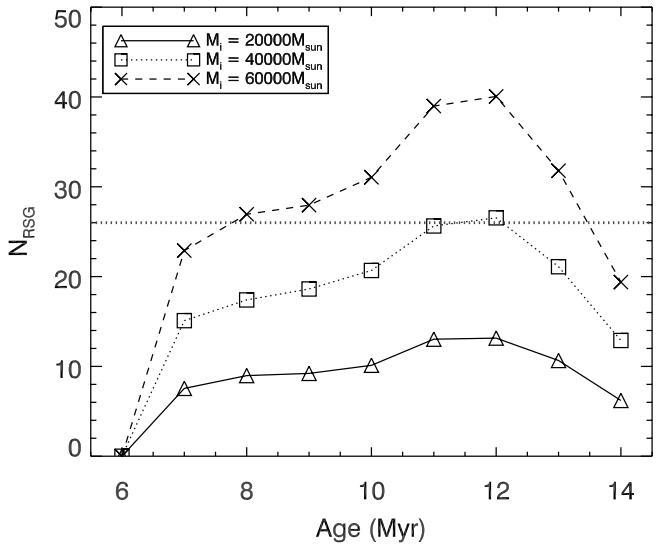

FIG. 15.—Number of RSGs in a cluster as a function of age for three different initial cluster masses, as calculated from the nonrotating Geneva models of Schaller et al. (1992). The observed number of 26 RSGs is indicated by the red dotted line. [*See the electronic edition of the Journal for a color version of this figure.*]

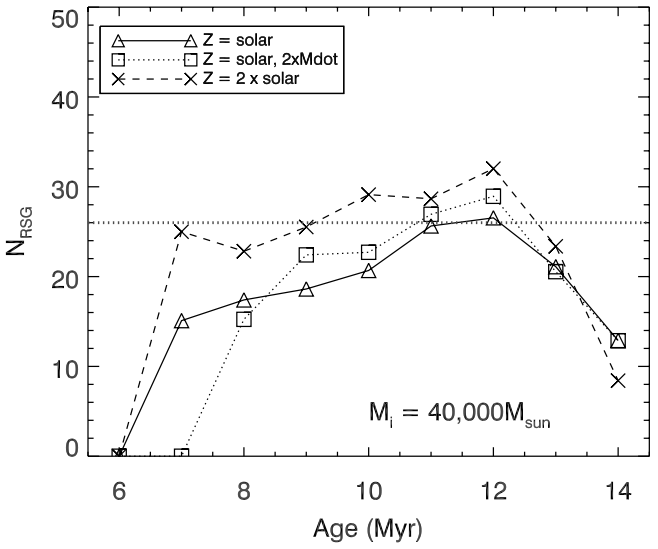

FIG. 16.—Number of RSGs in a cluster as a function of age for an initial cluster mass of $M_{\rm initial} = 4 \times 10^4\ M_\odot$, as calculated from the nonrotating models of Schaerer et al. (1993) and Meynet et al. (1994). Three different evolutionary tracks are investigated: solar metallicity with canonical mass-loss rates; solar metallicity with doubled mass-loss rates; and twice-solar metallicity. The observed number of 26 RSGs is indicated by the red dotted line. [*See the electronic edition of the Journal for a color version of this figure.*]

found that adjusting the position of the cluster center by $\pm 0.5'$ did not significantly affect this value with respect to the quoted uncertainty.

Density parameter, η.—As we do not have extensive data on many stars in the cluster (the RSGs are the only stars of which we can be sure are cluster members), measuring the η-parameter is beyond the scope of this work. For now, we use the canonical value of 10, which was shown be Spitzer (1987) to be valid for a range of models.

Using these values and their associated uncertainties, we find a dynamical cluster mass for RSGC2 of $(6 \pm 4) \times 10^4 (\eta/10)\ M_\odot$, assuming the kinematic cluster distance of 5.83 kpc. Below we compare this value to that found from comparison with theoretical isochrones.

4.1.2. *Evolutionary Models*

Following the Monte Carlo method of FMR06, we generate a coeval cluster of stars with a predefined total cluster mass and with initial stellar masses drawn randomly from a sample consistent with a Salpeter IMF (Salpeter 1955). For a given cluster age, we use the synthetic isochrones created from Geneva nonrotating stellar evolutionary tracks and determine the present-day luminosities and temperatures of the stars in the cluster. We isolate the supergiants as those stars with $\log (L_\star/L_\odot) > 4.5$, and define the red, yellow, and blue supergiants as those with temperatures ($T_{\rm eff} < 4500$ K, 4500 K $< T_{\rm eff} <$ 9000 K, and $T_{\rm eff} >$ 9000 K, respectively. We then count the numbers of RSGs for each simulated cluster for a given age and initial mass. Each simulation is repeated 10^3 times to reduce statistical error. We note that while the statistical uncertainty in the mean number of RSGs per model cluster is negligible, the 1 σ standard deviation of the mean is around 20% (FMR06). Hence cluster parameters that result in $N_{\rm RSG} = 26$ can produce $20 \lesssim N_{\rm RSG} \lesssim 32$ for a given trial.

In Figure 15 we plot the number of RSGs in a coeval cluster of a given initial mass as a function of age. For this plot we use the isochrones with solar metallicity and canonical mass-loss rates of Schaller et al. (1992). At ages below ~7 Myr, very few RSGs are present. The massive stars that have evolved off the MS experience high mass loss in the BSG phase, which prevents their evolution to the red. RSGs begin to appear when those stars with $M_{\rm initial} \sim 25\ M_\odot$ finish core-hydrogen burning. The number of RSGs then falls off rapidly above ~14 Myr as the stars massive enough to become RSGs exhaust their nuclear fuel. Hence, the likelihood of observing a cluster of 26 RSGs is much higher for cluster ages in the range 7–13 Myr.

Figure 15 illustrates that for coeval clusters, only those with $M_{\rm initial} \sim 4 \times 10^4\ M_\odot$ can produce numbers of RSGs in excess of 26, the number we observe in this cluster for the evolutionary models used in Figure 15. In Figure 16 we investigate the effect of using isochrones generated with different evolutionary tracks. We plot the results of using isochrones with solar metallicity and canonical mass-loss rates (as used in Fig. 15), solar metallicity with doubled mass-loss rates (Meynet et al. 1994), and twice-solar metallicity. While the different models produce slightly different results, in the likely range of cluster ages of 7–13—the model differences are smaller than the statistical variations of individual simulations. We therefore consider this to be a negligible source of uncertainty in this estimate of the cluster mass.

Much progress has been made in recent years in incorporating rotation in stellar structure codes (see review of Maeder & Meynet 2000), so a discussion of the effects of including rotation on our analysis seems warranted. Heger & Langer (2000), Meynet & Maeder (2000), and Heger et al. (2000) studied specifically the effect of rotation on stars in the initial mass range relevant to this work, i.e., $M_\star \sim 15$–$25\ M_\odot$. The broad result was that rotationally enhanced mixing increases the chemical homogeneity of the star, leading to larger helium cores, higher luminosities ($\Delta \sim 0.25$ dex), and lower effective temperatures ($\Delta \sim 400$ K) of RSGs. In addition, stars spent longer on the main sequence (~12%), due to the decreased effective gravity causing the star behave as a nonrotating star with lower initial mass.

In Figure 17 we investigate the effect of using the contemporary Geneva models, which include stellar rotation. The rotational velocity grids of these models are, as yet, not complete. Here we use the $v_i = 300$ km s^{-1} models, which are likely too large for this mass range and metallicity. However, they serve to investigate

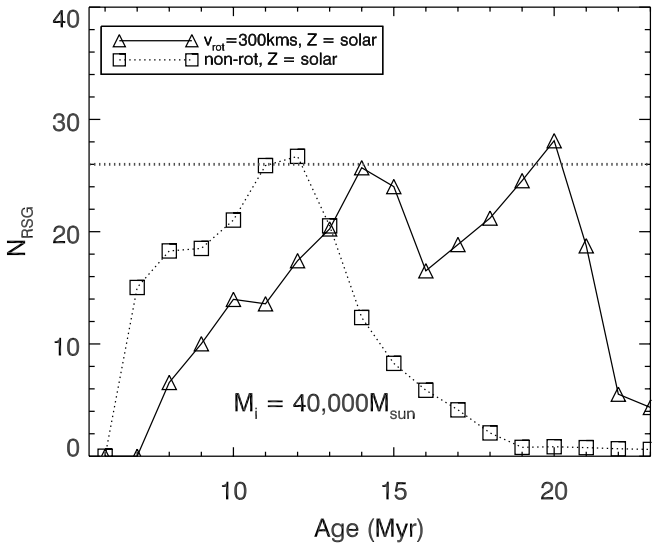

FIG. 17.—Same as Fig. 16, comparing the nonrotating solar metallicity models of Schaerer et al. (1993) with the fast-rotating, solar metallicity models of Meynet & Maeder (2000). [*See the electronic edition of the Journal for a color version of this figure.*]

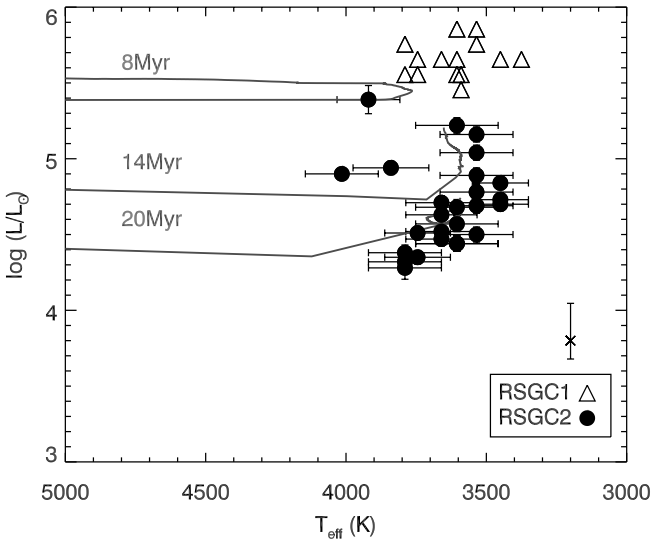

FIG. 18.—H-R diagram, showing the positions of the stars in the two Scutum RSG clusters. Also shown are isochrone fits for each cluster, based on rotating Geneva models with solar metallicity, canonical mass-loss rates, and initial rotational velocity of 300 km s^{-1}. As the RSGC2 stars are all at the same distance, the uncertainties shown in L_{bol} for these stars do not include the error in the cluster distance. The magnitude of the distance error is indicated separately in the bottom right of the panel. [*See the electronic edition of the Journal for a color version of this figure.*]

the impact of stellar rotation on our analysis. As the impact of rotation is greatest on the evolution of massive stars, due to its effect on the mass-loss behavior, Geneva models are only computed down to 9 $M_\odot$. To construct isochrones we spline together the massive, rotating models with the nonrotating models of mass <9 $M_\odot$.

The Figure 17 shows that, in the early part of the diagram ($\lesssim$15 Myr), the rotating models lag the nonrotating models, due to the longer time spent on the main sequence. At later times, the rotating models continue to produce RSGs long after the nonrotating models. This can be understood as a combination of longer lifetimes, and the stars' increased luminosity and decreased T_{eff}, enabling them to spend longer in the RSG "zone," as defined by our somewhat arbitrary thresholds of $\log(L/L_\odot) \geq 4.0$ and $T_{eff} \leq 4500$ K. The inclusion of rotation does not affect the inferred lower limit to the initial cluster mass of $M_{initial} \sim 4 \times 10^4$ $M_\odot$.

From isochrone fitting (see next section), we are able to constrain the age of the cluster to 12 ± 1 Myr (nonrotating models) and 17 ± 3 Myr (fast-rotating models). From these results, we estimate an "evolutionary" cluster mass for RSGC2 of $M_{ev} = (4 \pm 1) \times 10^4$ $M_\odot$. The uncertainty takes into account the statistical variations of the Monte Carlo method, and the error in the cluster age. The estimate compares well to the dynamical mass of $M_{dyn} = (6 \pm 4) \times 10^4 (\eta/10)$ $M_\odot$.

4.1.3. *The Effect of Cluster Noncoevality*

The mass derived above assumes that the stars were created in a coeval starburst. The large extent of the association ($\sim$10 pc at a distance of 5.83 kpc), as well as the large luminosity spread (see § 4.2), may suggest a sustained starburst phase of several million years. While the large size may be explained by expansion due to nonvirial equilibrium (see Bastian & Goodwin 2006; § 4.1.1) and the luminosity spread due to shortcomings in evolutionary models (Massey & Olsen 2003; § 4.2), we nonetheless discuss the effect of noncoeval star formation on our derived total mass.

The effect of cluster noncoevality would be to convolve the curves shown in Figure 15 with a smoothing function characterized by the length of the starburst phase. Thus, as long as the starburst occurred on timescales much shorter than the mean age of the cluster, it would not significantly affect the number of RSGs observed at any one time. For an extended starburst phase of order the inferred age of the cluster, the number of RSGs at any one time for a given cluster mass would decrease. Hence, a prolonged starburst would imply a larger cluster mass than derived here. The presence of main-sequence O stars or W-Rs, which have lifetimes of $\sim$3 Myr, or low-mass AGB stars with lifetimes of $\gg$20 Myr, would imply a sustained star-forming episode. Observations of such stars would require precise radial velocity measurements, such as those presented here, to confirm that they were part of the physical association.

4.2. *Cluster Age*

A novel method for estimating the age of a cluster from the RSG population was presented in FMR06. They showed that, using the nonrotating Geneva models, the luminosity range of RSGs for a coeval cluster changes with age (see their Fig. 19). For young ($\lesssim$7 Myr) clusters, the RSGs result from stars which have evolved horizontally across the HR diagram, meaning that the RSGs occupy a very narrow luminosity range. For older clusters, however, the RSGs—which result from stars of lower initial mass—have a larger luminosity spread, due to the upturn at the end of the evolutionary path (see Fig. 18).

The RSGC2 stars have luminosities ranging from $\log(L/L_\odot) = 4.2 \rightarrow 5.2$ (see Table 2). This compares to the larger luminosities and narrower spread of RSGC1, which has $\log(L/L_\odot) = 5.0 \rightarrow 5.6$. This can be seen clearly in Figure 18, which shows the locations of the stars in the two clusters on a H-R diagram. The luminosities of the stars in RSGC1 are taken from FMR06, and have been corrected for the slightly greater distance determined from SiO maser emission by Nakashima & Deguchi (2006) and the contemporary Galactic rotation curve (see above). Isochrone fits to the data, again using the fast-rotating Geneva models of Meynet & Maeder (2000) illustrate the clear age difference of the clusters. An age of 17 ± 3 Myr is consistent for RSGC2, compared to 8 ± 1 Myr for RSGC1. When nonrotating isochrones are used, the inferred age of RSGC2 becomes 12 ± 1 Myr, while the age of RSGC1 is unchanged. The figure shows that, while there

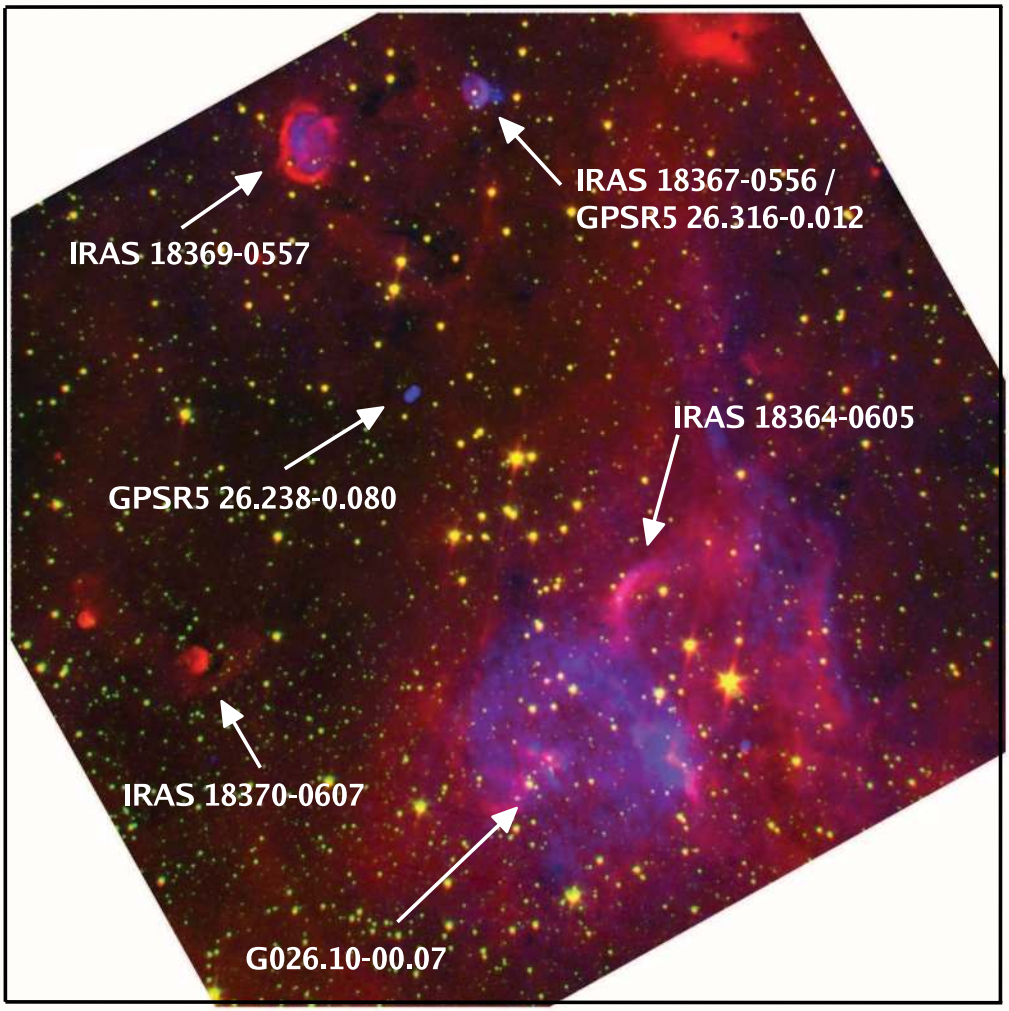

FIG. 19.—RGB composite image of the region around RSGC2. The image shows the *Spitzer* GLIMPSE bands 8.0 μm (*red*), 4.5 μm (*green*), and MAGPIS 20 cm (*blue*). Sources identified in radio surveys, as well as the likely origin of several *IRAS* point sources, are marked on the image.

may be some overlap in the absolute uncertainties, there is a clear age gap between the two clusters of several Myr.

While it is remarkable how the RSGC2 stars tightly follow the "hockey stick" end to the isochrone, no single isochrone reproduces the luminosity spread of the stars, with the 20 Myr rotating isochrone not extending to the greatest luminosities observed in the cluster. Taking Figure 18 at face value, this could imply that the cluster is noncoeval, and formed over a period of 6 Myr. However, it was a well-known problem that the nonrotating evolutionary models did not reproduce the highest observed luminosities of RSGs (Massey & Olsen 2003); and while the inclusion of rotation in evolutionary codes does in general make RSGs redder and brighter, it is not clear that the difference between observation and expectation has been completely reconciled. Indeed, the RSGCs may be the ideal laboratory in which to test these models.

4.3. *Unidentified Objects Near RSGC2: Evidence of Recent Starburst Activity at the Base of the Scutum-Crux Arm*

From the derived distances to the two RSG clusters, their separation is of order 100 pc. The proximity of these two remarkable objects to one another, combined with their similar ages, is perhaps indicative of a wider scale starburst episode in the region of the Scutum-Crux spiral arm. As noted by Nakashima & Deguchi (2006), the inferred distances for the objects put them close to where the spiral arms meet the Galactic bulge, roughly the corotation radius of the bulge bar (Bissantz et al. 2003), and in the middle of the proposed high-density "stellar ring" (Bertelli et al. 1995). The physical conditions and gas dynamics in this region of the Galaxy may precipitate star formation activity, while the location of the clusters within one of the corotation Lagrangian points (Englmaier & Gerhard 1999) may harbor the clusters from tidal disruption.

As we are looking tangentially along the Galactic arm at the point where it meets the bulge, it is reasonable to assume that there may be other evidence of recent star formation along our line of sight toward the two clusters. Indeed, separate from the cluster stars, there appear to be further RSGs in the direction of RSGC2. These objects have CO equivalent widths too large to be giants, but their radial velocities are inconsistent with being part of the cluster itself. These stars may be part of smaller clusters formed in a regionwide starburst phase around $\sim$10–20 Myr ago.

FMR06 discussed the possibility that various unidentified high-energy/radio sources in the region of RSGC1 were due to recent supernova activity, although the nonthermal radio-sources have since been shown to be extragalactic (Trejo & Rodríguez 2006). Here we make a similar discussion of the unidentified sources near RSGC2, using the Galactic plane survey data of GLIMPSE, MIPSGAL, and MAGPIS (Benjamin et al. 2003; Carey et al. 2005; Helfand et al. 2006).

Figure 19 shows a composite of IRAC channels 2 (4.5 μm) and 4 (8.0 μm), and *VLA*−20 cm, centered on RSGC2. The

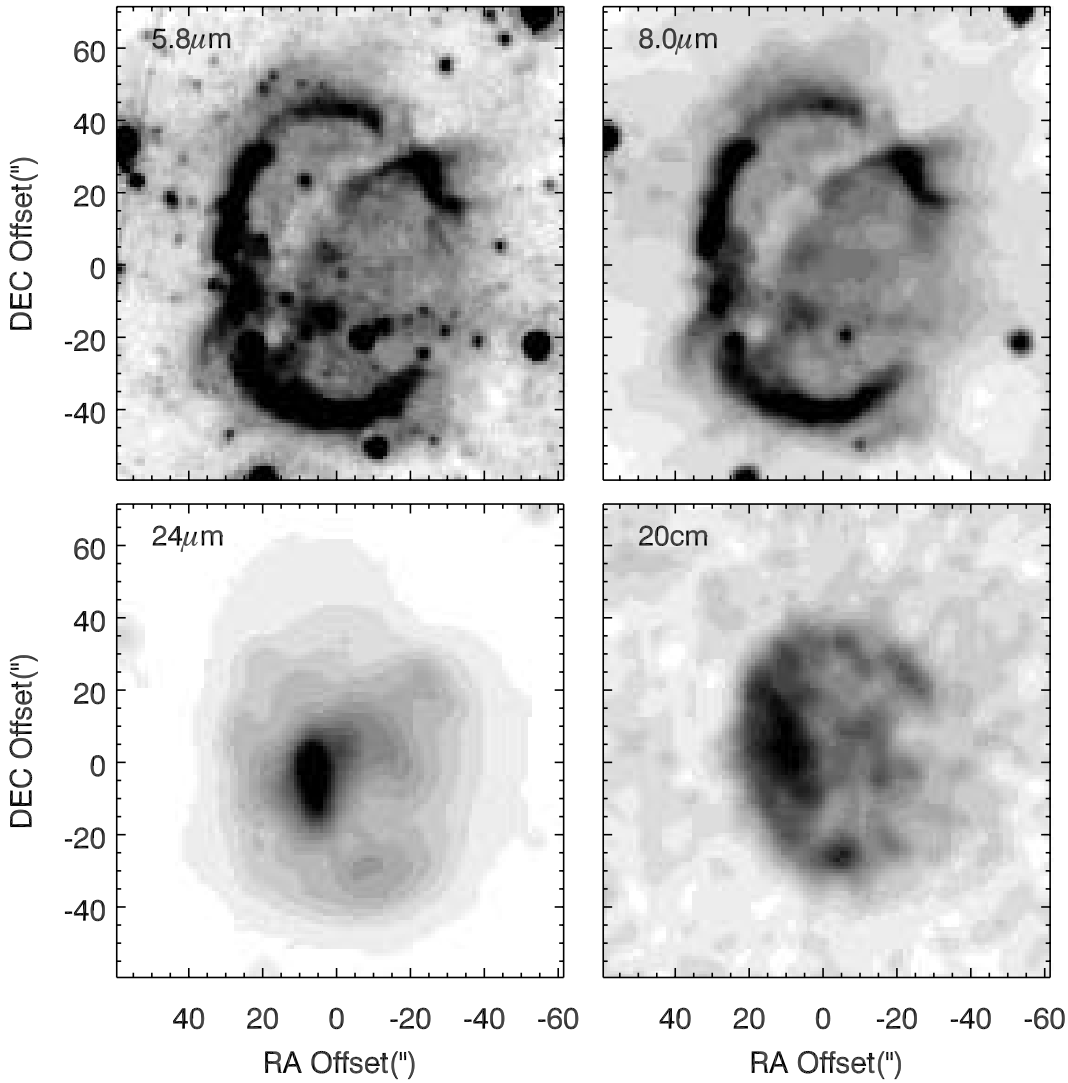

FIG. 20.—High-resolution images of the IRAS 18369−0557 source. *Top left*: *Spitzer* IRAC 5.8 μm; *top right*: *Spitzer* IRAC 8.0 μm; *bottom left*: MIPS 24 μm; and *bottom right*: VLA 20 cm. All images are scaled linearly between 0–7 σ above the sky background.

image shows in detail for the first time several radio and *IRAS* point sources, as well as the H II region G26.10−0.07. Below, we discuss the nature of each of these objects, as well as their relation to RSGC2 and the starburst phase in which it was created.

4.3.1. *IRAS 18369−0557*

When seen in detail (see images in Fig. 20), this object has the appearance of a discrete ring of material, which seems to peak in the 5.8 and 8 μm bands. Inside this ring is filled in with 20 cm emission, and the inner material is also bright at 24 μm such that it saturates the MIPSGAL image. The object is not detected in 2MASS, nor is it detected in IRAC bands 1 or 2. No obvious central point source is observed in any band. Aside from the bright ring, there is also a dark arc extending from the southeast to the northwest. This arc may be due to cold dust, oriented in some polar outflow perpendicular to the bright ring.

That the ring is so bright at 5.8 μm but not seen at 4.5 μm, with the central region peaking at ∼24 μm, suggests that the emission may be due to warm (∼100 K) dust, with strong PAH emission at 5 μm in the outer ring. Detailed temperature modeling of the dust would benefit from mid-IR spectroscopy across the nebula, such a study is beyond the scope of the current work.

From the object's appearance and the apparent lack of any central source, it is tempting to classify the object as a supernova remnant (SNR). The semimajor axis of the ring is 1.5′ across, which at the distance of RSGC2 corresponds to a diameter of 2.5 pc. If we assume a typical SN expansion speed of ∼1000 km s^{-1}, this would make the remnant ∼2500 years old *if* the dust has formed out of the SN ejecta. It would seem unlikely that 100 K dust would survive this long; by comparison, Blair et al. (2007) find that Kepler's SNR, which is ∼4 kpc away and ∼400 years old, is already very faint at 5.8 μm. A more likely explanation is that the dust was produced in a pre-SN mass-losing phase of the precursor, and has been heated by the SN explosion, which must have occurred less than a few hundred years ago. Such a situation is seen to be happening in SN 1987A (Bouchet et al. 2006).

It was argued in FMR06, using evolutionary models, that a cluster similar to RSGC1 should experience SNe explosions every ∼40,000–80,000 yr. For RSGC2, which appears to be 50% more massive but a little older, the corresponding timescale is around 50,000 yr. If a SN remnant takes around 10^4 yr before it becomes too faint to observe, then it is not unreasonable to assume that we may observe one recent supernova in a cluster like RSGC2. We note that at present there is currently no associated

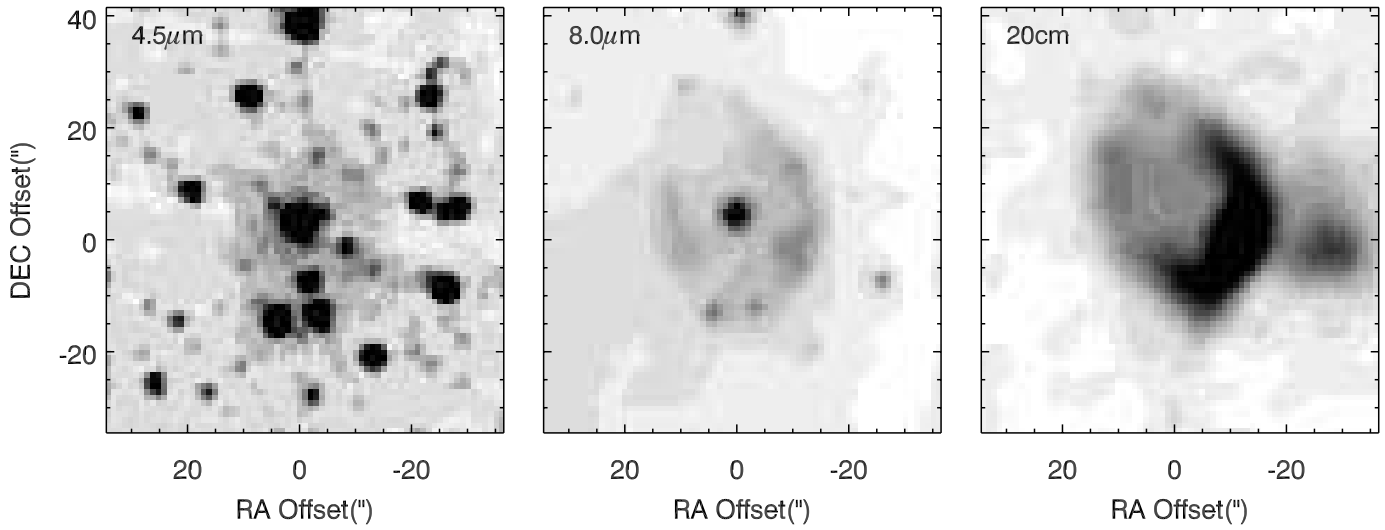

FIG. 21.—High-resolution images of the IRAS 18367−0556 source. *Left*: *Spitzer* IRAC 4.5 μm; *center*: *Spitzer* IRAC 8.0 μm; *right*: VLA 20 cm. All images are scaled linearly between 0–10 σ above the sky background.

high-energy source, and so classification of the object would benefit from X-ray/γ-ray observations.

4.3.2. *IRAS 18367−0556/GPRS5 26.316−0.012*

This object is another radio-bright, 8 μm–bright ring nebula, this time with a highly reddened star at the center ($H - K_s = 1.7$). The GLIMPSE and MAGPIS images of the object are shown in Figure 21. It is so bright at 24 μm that it saturates the corresponding MIPSGAL image. The object is reminiscent of an evolved star surrounded by the ejecta of a previous high mass-losing phase, such as a post-AGB star, an LBV, or a W-R star. Indeed, it is reminiscent of the mid-IR ring-nebulae seen around candidate LBVs in the *MSX* survey (Clark et al. 2003), in particular G26.47+0.02.

The radio source is detected in the 1.4 GHz NRAO VLA Sky Survey (NVSS; Condon et al. 1998), and has a flux of 65.6 ± 2 mJy. However, the source is flagged in the survey as being "complex," possibly due to the size of the source ($\sim$40″) being comparable to the size of the beam (FWHM = 45″). From Figure 21 it appears that the bulk of the radio emission is coincident with the southwestern part of the dust ring, rather than with the central star. It is therefore unlikely that the radio emission results from the ionized stellar wind, as one would expect to see emission from the base of the wind coincident with the central star. The radio emission could be explained by a hot central star ionizing the surrounding ejecta, or the fast wind of a hot phase plowing into a slower, dusty wind ejected when the star was cooler.

The object is very reminiscent of the LBV candidate HD 168625 (Robberto & Herbst 1998), speculated by Smith (2007) to be a Galactic analog of the progenitor of SN 1987A, based on the recent discovery of an 8 μm ring around the star. Clearly, further study of IRAS 18367−0556 is warranted, in particular near-IR spectroscopy to determine the stellar temperature, compare the star's radial velocity with the nearby RSG cluster, and to potentially determine abundances of Fe and α-group elements in this region of the Galaxy (see, e.g., the introduction of Najarro et al. 2004).

4.3.3. *GPSR5 26.238−0.080*

This is an extremely compact radio source, with no obvious counterpart in 2MASS, GLIMPSE, or MIPSGAL. For this reason, we suspect this source may be extragalactic.

4.3.4. *IRAS 18370—0607*

From the GLIMPSE-8 μm image, this object and the object just to the northeast appear to be either postmerger galaxies, or pinwheel nebulae as seen in interacting binary systems. That there are two such objects close together seems to favor the former explanation, although the extinction through this region of the Galaxy would mean that these objects were extremely intrinsically bright. For now we draw no definite conclusions as to the nature of these objects.

4.3.5. *G026.10−00.07*

This source was observed in the radio survey of Downes et al. (1980), who measured radial velocities of 33 km s^{-1} from H110α and 104 km s^{-1} from H_2CO. It would seem likely that the object as seen in Figure 19 is a foreground H II-region, and the H_2CO beam was contaminated by emission from the RSGs.

Wink et al. (1982) determine that for near- and far-side kinematic distances of the object, using the velocity measured by Downes et al. (1980) the rate of Lyman continuum photons absorbed is $\log(N_{\rm Ly}/s) = 48.54/50.08$. As the far-side distance would imply an extraordinarily massive cluster of $\sim$8 O3 stars (e.g., Sternberg et al. 2003), and as no obvious central cluster is seen, the nearside distance seems more likely.

4.3.6. *Star 1, Star 49, and IRAS 18364-0605*

It can be seen from Figure 22 that star 49 has remarkable near- and mid-IR excess. In addition, the IRAC images show the star apparently at the center-of-curvature of a bow-shock structure, identified in the *IRAS* point-source catalog as IRAS 18364−0605. Star 49 itself is one of the most luminous stars in the cluster, while having an earlier than average spectral type (K3). The star's temperature places it close to the yellow hypergiants, a short evolutionary phase experienced by stars on their way from the RSG to the LBV/W-R stages (de Jager 1998). In clusters containing so many RSGs, it is not unreasonable to expect to find one such object (see also star 15 in RSGC1; FMR06).

Star 49 is not as hot as the yellow hypergiants; however, the large IR-excess is suggestive of large amounts of warm circumstellar dust ejected in a high mass losing episode, possibly a precursor to blueward evolution. It would be interesting to measure the mass-loss rate of this object and compare it to that of

outburst of the yellow hypergiant IRC +10 420, during which the mass-loss rate is inferred to have reached $5 \times 10^{-4}\ M_{\odot}\mathrm{yr}^{-1}$ (Oudmaijer et al. 1996). Since evolved then the star has apparently evolved to an A-type supergiant (Klochkova et al. 2002), although this may be due to the dissipation of the pseudophotosphere created by the dense wind (Smith et al. 2004).

Star 1 is by far the brightest object in this field in the *K*-band ($K_s = 2.9$), and is highly reddened ($H - K_s = 1.798$). It is not possible to fit this star with a standard reddening law, assuming the late spectral type of M5–M6 derived from its CO band-head absorption. It is likely this object has significant IR excess, possibly due to an extreme mass-losing episode. Its radial velocity is $\sim$20 km s^{-1} below that of the rest of the "cluster" stars, hence it is unlikely to be a foreground giant. Indeed, the star may be part of the RSGC2 cluster, and its observed radial velocity offset by an expanding optically thick envelope; the velocity difference of $\sim$20 km s^{-1} is a typical outflow speed for a RSG. It is possible that this star is an extreme red hypergiant, such VY CMa—a star with large IR excess and inferred mass-loss rate of $\sim 2 \times 10^{-4}\ M_{\odot}$ (Danchi et al. 1994).

The red and yellow hypergiants are extremely rare objects; however, it is not clear whether this is due to the exceptional nature of certain stars, or whether all stars of a particular initial mass range and metallicity will pass through brief but extreme mass-losing episodes such as these. If the latter is true, it is then not unreasonable to expect to find such stars among the two Scutum-Crux RSG clusters, as RSGC1 and RSGC2 appear to be of just the right age and initial mass. Stars 1 and 49 certainly warrant further study in the context of the evolution of RSGs at Galactic metallicity, as they appear to be on the verge of shedding their outer layers and evolving blueward toward the LBV/WN phases.

4.4. *The RSG Clusters in the Broader Context of Astrophysics*

From the cluster mass and age derived here, RSGC2 joins the nearby RSGC1 (FMR06), Wd 1 (Clark et al. 2005), the Arches (Figer et al. 2002), Quintuplet (Figer et al. 1999), and Galactic center (Figer et al. 2004) clusters, in a growing list of Galactic analogs to super–star clusters. These objects represent ideal natural laboratories in which to study the evolution of massive stars. The Arches cluster is massive enough and young enough to contain main-sequence O-stars up to the mass of $\sim$150 $M_{\odot}$ (Figer et al. 2002), while the age and mass of Wd 1 is tuned in such a way that it contains 24 W-R stars—8% of all those known in the Galaxy (Clark & Negueruela 2002; Negueruela & Clark 2005; Groh et al. 2006; Crowther et al. 2006). Meanwhile, Martins et al. (2007) recently applied abundance analysis to the unusually large number of Opfe/WN 9 stars in the Galactic center cluster to tie down their evolutionary status.

Of this collection of massive Galactic clusters, the two RSG clusters are evidently the elder, not only from the population-synthesis analysis presented here and in FMR06, but also from the lack of diffuse radio emission at the center of the clusters, and hence of few remaining hot main-sequence stars (we note that, while RSGC2 has a radio nebula just to the southwest, radio recombination line observations place this object in the foreground; see § 4.3).

This gives the two clusters a unique role in the context of massive stellar evolution, as they offer the opportunity to study a statistically significant population of RSGs and probe the evolution of stars in the mass-range of $\sim$15–25 $M_{\odot}$. Evidence is growing that such stars are the progenitors of Type II SNe (Van Dyk et al. 2003; Smartt et al. 2004), while they may contribute significantly toward Galactic-scale dust production, particularly in low-metallicity starbursts where carbon-sequence W-Rs are absent and AGB stars are yet to form (see discussion by Massey et al. 2005).

As hinted by the distribution of spectral types (§ 3.3), the clusters likely have similar abundances, representative of the rest of the Galaxy. In addition, the fact that there are *two* clusters, with slightly different ages—and hence initial masses of RSGs—now permits evolutionary studies at uniform metallicity, and as a function of initial mass.

4.4.1. *The RSGCs as a Probe of the Galactic Z-gradient*

Aside from the unusually large number of RSGs and the opportunities they present for studying stellar evolution, an additional interesting aspect of the clusters is their location in the Galactic plane at a Galactocentric distance of $\sim$4 kpc. Here they are close to where the disk meets the central bulge, within the proposed "ring" of enhanced stellar density (Bertelli et al. 1995).

Chemical abundance analyses of this region could be key to understanding the formation and evolution of our Galaxy, in the transition zone between the Galactic disk and bulge. An important constraint on models of the formation of the Galaxy and its central bulge is the radial metallicity gradient. Abundance analyses of H II regions, planetary nebulae, and early-type stars have found a steadily increasing metal content from 18–5 kpc (e.g., Afflerbach et al. 1997; Maciel & Quireza 1999; Rolleston et al. 2000). The metallicity within 5 kpc of the Galactic center is less clear: Smartt et al. (2001) find that the metallicity continues to increase at the same slope down to 2.5 kpc, although curiously not for oxygen, while studies of the inner $\sim$50 pc have have revealed roughly solar abundances (e.g., Ramírez et al. 2000; Najarro et al. 2004).

The RSGCs are now a powerful tool with which to probe what could potentially be the transition zone between the Galactic disk and bulge, and the location where the metallicity gradient breaks down. Near-IR spectral analyses of RSGs can yield Fe abundances (e.g., Rich & Origlia 2005), while analysis of the LBV candidate, and any BSGs in the clusters, would provide direct measurements of Fe and α-group elements such as Si and Mg (Najarro 2006).

5. CONCLUSIONS

Using near-IR spectroscopy, and 2MASS/GLIMPSE/*MSX* photometry, we have shown that there is a second reddened, massive young cluster of RSGs in the Galactic plane at $l = 25^{\circ}$–26°. We find that this cluster, RSGC2, contains 26 RSGs, almost twice as many as the nearby RSGC1. From evolutionary synthesis and kinematic measurements we infer that RSGC2 is slightly older and the more massive of the two, with a mass comparable to that of Westerlund 1. Together, the two Scutum-Crux RSG clusters harbor $\sim$20% of all known RSGs in the Galaxy, and now offer an unprecedented opportunity to study presupernova evolution at uniform metallicity. Further, new infrared/radio survey images reveal several background RSGs, and candidates for a supernova remnant and a luminous blue variable in the field of RSGC2. Along with the proximity of RSGC1, this suggests intense, recent, regionwide star formation activity at the point where the Scutum-Crux Galactic arm meets the Galactic bulge. Future abundance studies of this region would yield important information in the study of the Galactic metallicity gradient, and the interaction between the disk and the bulge.

We would like to thank the anonymous referee for a careful reading of the manuscript and several suggestions which improved the paper. For useful discussions we thank Simon Clark, and Tom Jarrett for discussions concerning the nature of IRAS

18370−0607. The material in this work is supported by NASA under award NNG 05-GC37G, through the Long-Term Space Astrophysics program. IRMOS is supported by NASA James Webb Space Telescope, NASA Goddard Space Flight Center, STScI DDRF, and KPNO. This research has made use of the SIMBAD database, Aladin and IDL software packages, and the GSFC IDL library. This research was performed in the Rochester Imaging Detector Laboratory with support from a NYSTAR Faculty Development Program grant. Some of the data presented herein were obtained at the W. M. Keck Observatory, which is operated as a scientific partnership among the California Institute of Technology, the University of California, and the National Aeronautics and Space Administration. The Observatory was made possible by the generous financial support of the W. M. Keck Foundation.

APPENDIX

In Figure 22 we plot the SEDs of the cluster stars.

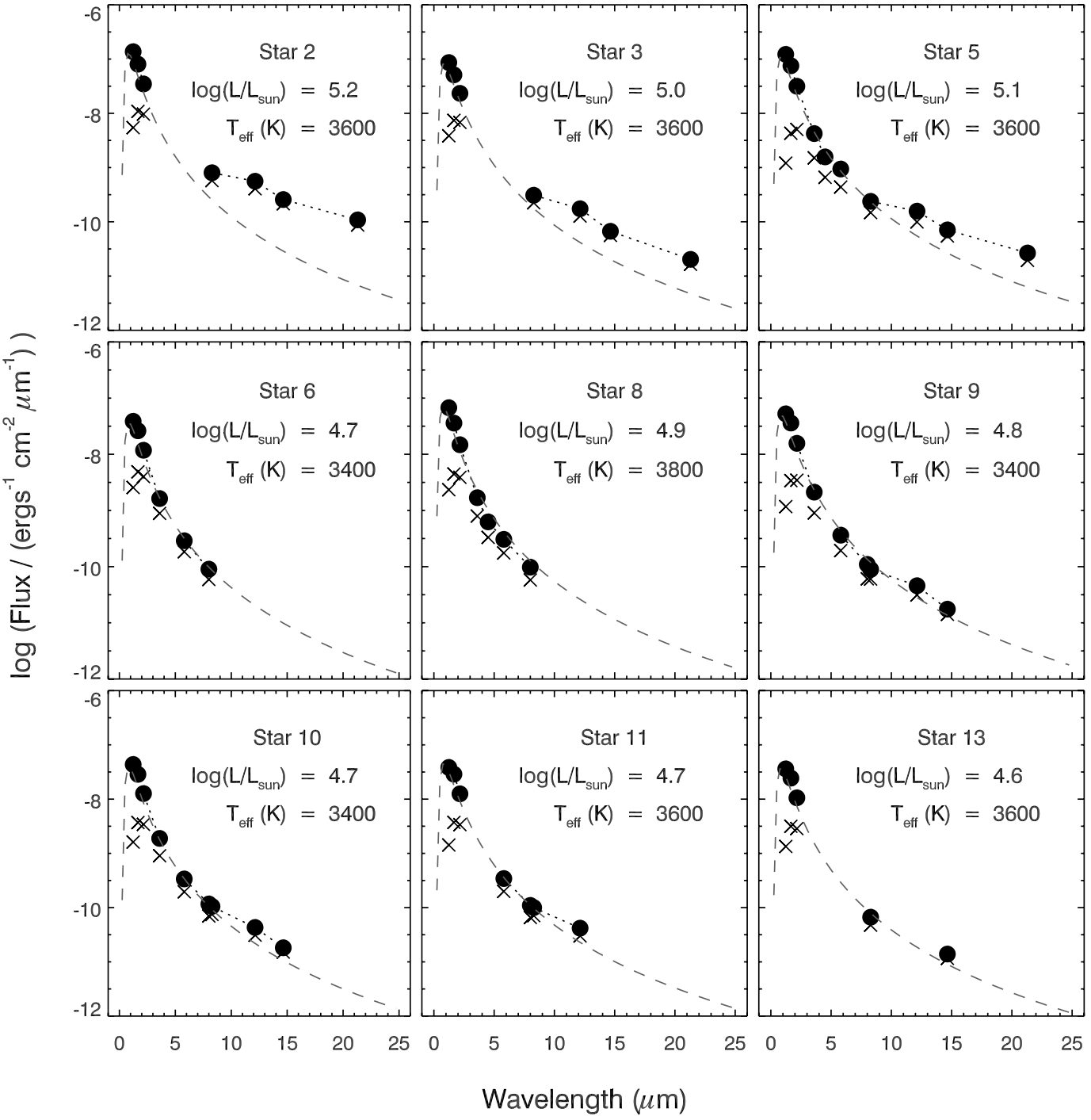

FIG. 22.—SEDs of the cluster members, using data from the point-source catalogs of 2MASS, GLIMPSE, and *MSX*. The raw photometry is plotted as crosses, and the dereddened photometry as filled circles. Neither GLIMPSE data below 5 σ nor *MSX* upper limit data are plotted. The green dotted line in each panel represents a blackbody curve appropriate for each star's K_s-band magnitude, reddening and temperature, and the kinematic distance to the cluster. We note that there may be some contamination in the *MSX* aperture between stars 2 and 6, which may explain the large mid-IR excess of star 2. [*See the electronic edition of the Journal for a color version of this figure.*]

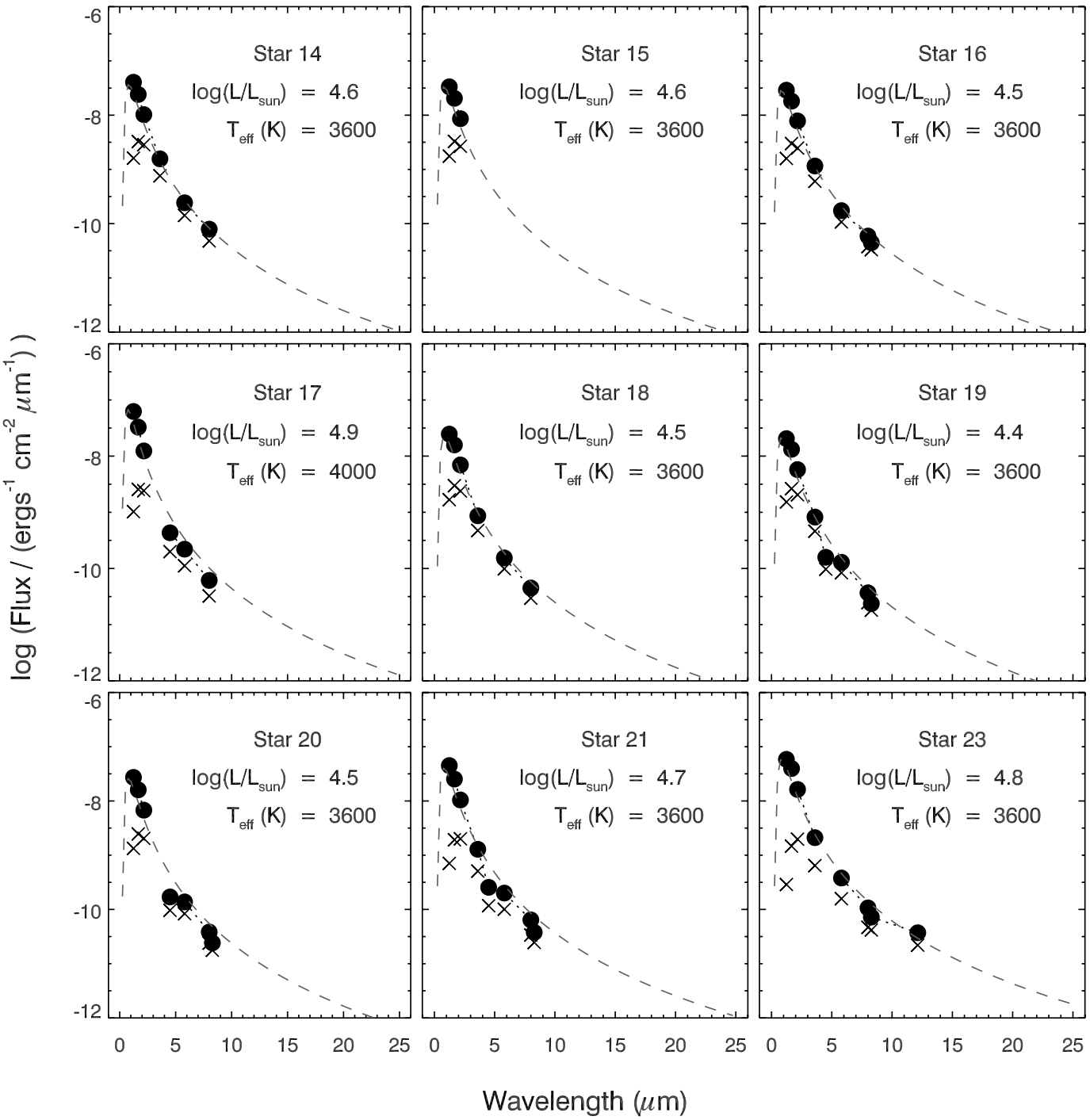

FIG. 22—*Continued*

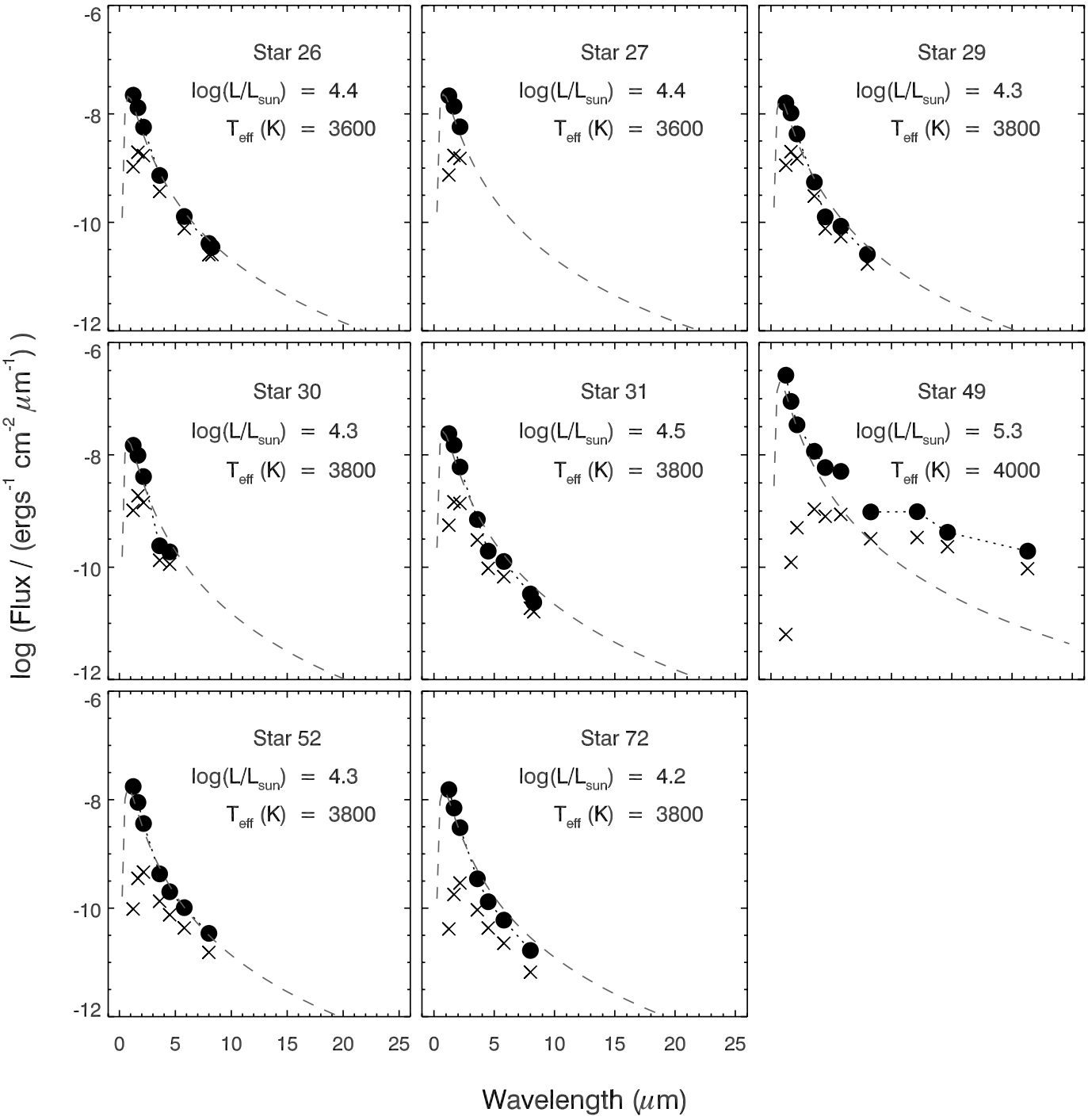

FIG. 22—*Continued*

REFERENCES

Afflerbach, A., Churchwell, E., & Werner, M. W. 1997, ApJ, 478, 190
Bastian, N., & Goodwin, S. P. 2006, MNRAS, 369, L9
Benjamin, R. A., et al. 2003, PASP, 115, 953
Bertelli, G., Bressan, A., Chiosi, C., Ng, Y. K., & Ortolani, S. 1995, A&A, 301, 381
Bica, E., Dutra, C. M., & Barbuy, B. 2003a, A&A, 397, 177
Bica, E., Dutra, C. M., Soares, J., & Barbuy, B. 2003b, A&A, 404, 223
Bissantz, N., Englmaier, P., & Gerhard, O. 2003, MNRAS, 340, 949
Blair, W. P., et al. 2007, ApJ, 662, 998
Bouchet, P., et al. 2006, ApJ, 650, 212
Buchanan, C. L., et al. 2006, AJ, 132, 1890
Carey, S. J., et al. 2005, in BAAS, 37, 1252
Caron, G., Moffat, A. F. J., St-Louis, N., Wade, G. A., & Lester, J. B. 2003, AJ, 126, 1415
Clark, J. S., et al. 2003, A&A, 412, 185
Clark, J. S., & Negueruela, I. 2002, A&A, 396, L25
Clark, J. S., Negueruela, I., Crowther, P. A., & Goodwin, S. P. 2005, A&A, 434, 949
Condon, J. J., et al. 1998, AJ, 115, 1693
Crowther, P. A., Hadfield, L. J., Clark, J. S., Negueruela, I., & Vacca, W. D. 2006, MNRAS, 372, 1407
Cutri, R. M., Skrutskie, M. F., van Dyk, S., et al. 2003, 2MASS All Sky Catalog of Point Sources (Pasadena: Caltech), http://irsa.ipac.caltech.edu/applications/Gator
Danchi, W. C., Bester, M., Degiacomi, C. G., Greenhill, L. J., & Townes, C. H. 1994, AJ, 107, 1469
de Jager, C. 1998, Astron. Astrophys. Rev., 8, 145
Downes, D., Wilson, T. L., Bieging, J., & Wink, J. 1980, A&AS, 40, 379
Dutra, C. M., Bica, E., Soares, J., & Barbuy, B. 2003, A&A, 400, 533
Egan, M. P., Price, S. D., & Gugliotti, G. M. 2001, in BAAS, 24, 561
Eisenhauer, F., et al. 2005, ApJ, 628, 246
Elias, J. H., Frogel, J. A., & Humphreys, R. M. 1985, ApJS, 57, 91
Englmaier, P., & Gerhard, O. 1999, MNRAS, 304, 512
Feast, M., & Whitelock, P. 1997, MNRAS, 291, 683
Figer, D. F., McLean, I. S., & Morris, M. 1999, ApJ, 514, 202
Figer, D. F., Rich, R. M., Kim, S. S., Morris, M., & Serabyn, E. 2004, ApJ, 601, 319
Figer, D. F., et al. 2002, ApJ, 581, 258
———. 2003, ApJ, 599, 1139
———. 2006, ApJ, 643, 1166 (FMR06)
Fluks, M. A., et al. 1994, A&AS, 105, 311
Groh, J. H., Damineli, A., Teodoro, M., & Barbosa, C. L. 2006, A&A, 457, 591
Heger, A., Fryer, C. L., Woosley, S. E., Langer, N., & Hartmann, D. H. 2003, ApJ, 591, 288
Heger, A., & Langer, N. 2000, ApJ, 544, 1016
Heger, A., Langer, N., & Woosley, S. E. 2000, ApJ, 528, 368
Helfand, D. J., Becker, R. H., White, R. L., Fallon, A., & Tuttle, S. 2006, AJ, 131, 2525
Humphreys, R. M. 1979, ApJ, 231, 384
Indebetouw, R., et al. 2005, ApJ, 619, 931
Josselin, E., Blommaert, J. A. D. L., Groenewegen, M. A. T., Omont, A., & Li, F. L. 2000, A&A, 357, 225
Kleinmann, S. G., & Hall, D. N. B. 1986, ApJS, 62, 501
Klochkova, V. G., Yushkin, M. V., Chentsov, E. L., & Panchuk, V. E. 2002, Astron. Rep., 46, 139
Kothes, R., & Dougherty, S. M. 2007, A&A, 468, 993
Kudritzki, R.-P., & Puls, J. 2000, ARA&A, 38, 613
Levesque, E. M., et al. 2005, ApJ, 628, 973
Maciel, W. J., & Quireza, C. 1999, A&A, 345, 629
MacKenty, J. W., et al. 2003, Proc. SPIE, 4841, 953
Maeder, A., & Meynet, G. 2000, A&A, 361, 159
Martins, F., et al. 2007, A&A, 468, 233
Massey, P., & Olsen, K. A. G. 2003, AJ, 126, 2867
Massey, P., et al. 2005, ApJ, 634, 1286
Maund, J. R., Smartt, S. J., Kudritzki, R. P., Podsiadlowski, P., & Gilmore, G. F. 2004, Nature, 427, 129
McLean, I. S., et al. 1998, Proc. SPIE, 3354, 566
Mengel, S., Lehnert, M. D., Thatte, N., & Genzel, R. 2002, A&A, 383, 137
Messineo, M., et al. 2005, A&A, 435, 575
Meynet, G., & Maeder, A. 2000, A&A, 361, 101
Meynet, G., Maeder, A., Schaller, G., Schaerer, D., & Charbonnel, C. 1994, A&AS, 103, 97
Najarro, F. 2006, J. Phys. Conf. Ser., 54, 224
Najarro, F., Figer, D. F., Hillier, D. J., & Kudritzki, R. P. 2004, ApJ, 611, L105
Nakashima, J.-I., & Deguchi, S. 2006, ApJ, 647, L139
Nakaya, H., Watanabe, M., Ando, M., Nagata, T., & Sato, S. 2001, AJ, 122, 876
Negueruela, I., & Clark, J. S. 2005, A&A, 436, 541
Ortolani, S., Bica, E., Barbuy, B., & Momany, Y. 2002, A&A, 390, 931
Oudmaijer, R. D., Groenewegen, M. A. T., Matthews, H. E., Blommaert, J. A. D. L., & Sahu, K. C. 1996, MNRAS, 280, 1062
Ramírez, S. V., et al. 2000, ApJ, 537, 205
Reid, M. J., & Brunthaler, A. 2004, ApJ, 616, 872
Rich, R. M., & Origlia, L. 2005, ApJ, 634, 1293
Rieke, G. H., & Lebofsky, M. J. 1985, ApJ, 288, 618
Robberto, M., & Herbst, T. M. 1998, ApJ, 498, 400
Rolleston, W. R. J., Smartt, S. J., Dufton, P. L., & Ryans, R. S. I. 2000, A&A, 363, 537
Salpeter, E. E. 1955, ApJ, 121, 161
Schaerer, D., Charbonnel, C., Meynet, G., Maeder, A., & Schaller, G. 1993, A&AS, 102, 339
Schaller, G., Schaerer, D., Meynet, G., & Maeder, A. 1996, A&A, 96, 269
Smartt, S. J., et al. 2001, A&A, 367, 86
———. 2004, Science, 303, 499
Smith, N. 2007, AJ, 133, 1034
Smith, N., Vink, J. S., & de Koter, A. 2004, ApJ, 615, 475
Sonneborn, G., Altner, B., & Kirshner, R. P. 1987, ApJ, 323, L35
Spitzer, L. 1987, Dynamical Evolution of Globular Clusters (Princeton: Princeton Univ. Press)
Stephenson, C. B. 1990, AJ, 99, 1867
Sternberg, A., Hoffmann, T. L., & Pauldrach, A. W. A. 2003, ApJ, 599, 1333
Trejo, A., & Rodríguez, L. F. 2006, Rev. Mex. AA, 42, 147
Van Dyk, S. D., Li, W., & Filippenko, A. V. 2003, PASP, 115, 1289
van Loon, J. T., Cioni, M.-R. L., Zijlstra, A. A., & Loup, C. 2005, A&A, 438, 273
Wallace, L., & Hinkle, K. 1996a, ApJS, 103, 235
———. 1996b, ApJS, 107, 312
———. 1997, ApJS, 111, 445
Whitelock, P., et al. 1994, MNRAS, 267, 711
Wink, J. E., Altenhoff, W. J., & Mezger, P. G. 1982, A&A, 108, 227